

UCLA

UCLA Previously Published Works

Title

Extracellular domains of CARs reprogramme T cell metabolism without antigen stimulation.

Permalink

<https://escholarship.org/uc/item/1zq4c2sz>

Journal

Nature Metabolism, 6(6)

Authors

Lakhani, Aliya

Chen, Ximin

Chen, Laurence

[et al.](#)

Publication Date

2024-06-01

DOI

10.1038/s42255-024-01034-7

Peer reviewed



Published in final edited form as:

Nat Metab. 2024 June ; 6(6): 1143–1160. doi:10.1038/s42255-024-01034-7.

Extracellular Domains of CARs Reprogram T-Cell Metabolism without Antigen Stimulation

Aliya Lakhani¹, Ximin Chen¹, Laurence C. Chen¹, Mihe Hong¹, Mobina Khericha², Yu Chen³, Yvonne Y. Chen^{1,2,4,5}, Junyoung O. Park^{1,4,*}

¹Department of Chemical and Biomolecular Engineering, University of California, Los Angeles, Los Angeles, CA 90095, USA

²Department of Microbiology, Immunology, and Molecular Genetics, University of California, Los Angeles, Los Angeles, CA 90095, USA

³Department of Chemistry and Biochemistry, University of California, Los Angeles, Los Angeles, CA 90095, USA

⁴Jonsson Comprehensive Cancer Center at UCLA, Los Angeles, CA 90095, USA

⁵Parker Institute for Cancer Immunotherapy Center at UCLA, Los Angeles, CA 90095, USA

Abstract

Metabolism is an indispensable part of T-cell proliferation, activation, and exhaustion, yet the metabolism of chimeric antigen receptor (CAR)-T cells remains incompletely understood. CARs are comprised of extracellular domains—often single-chain variable fragments (scFvs)—that determine ligand specificity, and intracellular domains that trigger signaling upon antigen binding. Here, we show that CARs differing only in the scFv variously reprogram T-cell metabolism. Even without exposure to antigens, some CARs increase proliferation and nutrient uptake in T cells. Using stable isotope tracers and mass spectrometry, we observed basal metabolic fluxes through glycolysis doubling and amino acid uptake overtaking anaplerosis in CAR-T cells harboring a rituximab scFv, unlike other similar anti-CD20 scFvs. Disparate rituximab and 14g2a-based anti-GD2 CAR-T cells are similarly hypermetabolic and channel excess nutrients to nitrogen overflow metabolism. Modest overflow metabolism of CAR-T cells and metabolic compatibility between cancer and CAR-T cells are identified as features of efficacious CAR-T cell therapy.

*Correspondence: jop@ucla.edu.

Author Contributions

A.L. and J.O.P. designed the study and wrote the paper with feedback from Y.Y.C. A.L., X.C., L.C.C., M.H., M.K., Y.C., and J.O.P. carried out the experiments. X.C., L.C.C., M.H., and M.K. generated CAR-T cells. A.L. measured nutrient uptake and byproduct secretion rates. X.C. and M.H. measured exhaustion and activation markers. L.C.C. performed RNA-seq. X.C. conducted *in vivo* experiments. A.L. and Y.C. performed phosphopeptide measurement. A.L. and J.O.P. performed metabolomics and metabolic flux analysis. A.L. and J.O.P. performed integral analysis of metabolomic, transcriptomic, and functional data using thermodynamic and metabolic control frameworks.

Code availability

The code for metabolic flux analysis, nutrient uptake and byproduct secretion measurement, and statistical analysis is available on the GitHub public repository: <https://github.com/aliyalakhani/CAR-T-Cell-Metabolism>

Introduction

Chimeric antigen receptors (CARs) are synthetic proteins that activate T cells upon binding cognate antigens¹. CAR-T cell therapies targeting CD19 or B-cell maturation antigen (BCMA) have received FDA approval for the treatment of B-cell leukemia and lymphoma or multiple myeloma, respectively²⁻⁴. Despite recent successes, the design of new CARs relies on heuristics rather than quantitative metrics⁵.

Metabolism fuels T cells by supplying cellular energy and biochemical building blocks necessary for proliferation, cytokine production, and cytotoxicity. The inner workings of T-cell metabolism have become increasingly accessible due to improvements in analytical techniques such as electrochemical probes, NMR, and mass spectrometry⁶⁻⁸. Upon activation, T cells undergo metabolic reprogramming to meet the increased energetic and biosynthetic demands⁹. Naïve T cells are metabolically quiescent; they have slow glycolysis and rely more on fatty acid oxidation and oxidative phosphorylation to produce ATP⁹. The initiation of T-cell activation is triggered by T-cell receptor (TCR) signaling and costimulation, resulting in T-cell proliferation, differentiation, and production of effector molecules like cytokines¹⁰. TCR activation also triggers signaling pathways that lead to increased glucose uptake^{9,10}. Activated T cells use the increased glucose flux to support energy metabolism, the pentose phosphate pathway (PPP), one-carbon metabolism, and fatty acid synthesis^{11,12}. Similarly, when CAR-T cells encounter cognate antigens, they mount an immune response by increasing nutrient uptake and shifting to anabolism to support proliferation, differentiation, and effector functions^{9,13}. However, persistent antigen stimulation exhausts T cells by impairing oxidative phosphorylation and inducing mitochondrial oxidative stress to limit nucleotide biosynthesis and proliferative capacity¹⁴. These metabolic alterations impact anti-tumor responses and contribute to the development of terminal dysfunction in CAR-T cells¹⁴.

As different cancer targets require different CAR-T cells, we asked whether the choice of CAR would affect T-cell metabolism. The antigen specificity of the CAR molecule is dictated by its extracellular ligand-binding domain, which is most commonly a single-chain variable fragment (scFv). The scFv is a fusion protein that combines the variable regions of the heavy chain (V_H) and light chain (V_L) of an antibody. Within each variable region, the scFv is comprised of three complementarity-determining regions (CDRs) interspersed among four framework regions (FRs)⁵. CARs that are different only in their scFv domain but otherwise identical have been used to target diverse antigens and tumor types⁵. Previous studies have shown that the binding affinities of scFvs can affect the selectivity of CAR molecules by influencing the CAR-T cells' ability to distinguish target cells with different antigen expression levels¹⁵. However, if and how the choice of scFv in CAR protein design affects CAR-T cell metabolism remain unknown.

To answer this question, we characterized the basal metabolism of a panel of human T cells expressing each of seven (one anti-CD19, five anti-CD20, and one anti-GD2) CARs with identical transmembrane, costimulatory, and signaling domains using liquid chromatography-mass spectrometry (LC-MS). These CARs were chosen due to their clinical relevance. Like all currently FDA-approved CAR-T cell therapies targeting CD19, the

anti-CD19 scFv used in this study is derived from the FMC63 antibody¹⁶. Nonetheless, one of the reasons for cancer relapse and resistance after CAR-T cell treatment is antigen escape, a phenomenon in which cancer cells efface, mutate, and/or downregulate the targeted antigen¹⁷. Since both CD19 and CD20 are commonly expressed on B-cell lymphomas¹⁸, the latter has garnered interest as an alternative target for CAR-T cell therapy. Leu16 is an anti-CD20 monoclonal antibody (mAb) that has been clinically evaluated and has been reported as safe and highly efficacious in anti-CD20¹⁹ and anti-CD19/CD20 bispecific CAR-T cells²⁰. Rituximab anti-CD20 mAb is used as a standard component of care for multiple B-cell malignancies²¹. CARs incorporating Leu16 and rituximab scFvs as well as their hybrid RFR-LCDR (FRs from rituximab and CDRs from Leu16) and alanine-inserted CARs have been vetted for their *in vivo* efficacy²². We used anti-GD2 CAR-T cells based on 14g2a mAb, which are known for ligand-independent activation²³, as a positive control.

Even in the absence of antigens, the expression of CARs altered the proliferation and nutrient requirements of CAR-T cells. The nature of metabolic reprogramming was CAR-dependent. Using ¹³C and ¹⁵N tracers and quantitative flux modeling, we observed metabolic fluxes through glycolysis doubling and amino acid uptake increasing to overtake anaplerosis in CAR-T cells harboring a rituximab anti-CD20 scFv compared to control T cells lacking CAR expression. In contrast, CAR-T cells harboring anti-CD19 scFv and other anti-CD20 scFvs with high sequence identity to the rituximab scFv upregulated metabolic activities to a lesser extent. Interestingly, 14g2a anti-GD2 and rituximab anti-CD20 CAR-T cell variants with divergent scFv sequences exhibited similarly exorbitant nutrient requirements and metabolic fluxes. These hypermetabolic CAR-T cells used the excess amino acid intake to operate nitrogen overflow metabolism, secreting nucleobases, non-essential amino acids, and ammonia. The impact of the extracellular environment on T-cell proliferation depended on scFv-specific CAR-T cell metabolism. Ammonia addition decreased the proliferation rate of rituximab anti-CD20 CAR-T cells while alanine addition increased the proliferation of anti-CD19 and non-rituximab-based anti-CD20 CAR-T cells. In mice bearing Raji or Ramos lymphoma xenografts, the conjunction of modest waste secretion by CAR-T cells and metabolic compatibility between cancer and CAR-T cells was recognized as a desired feature. Since metabolism is fundamental to cellular function and proliferation and CAR domains alter T-cell metabolism, we propose the broad adoption of metabolic profiling and engineering as a critical step in the development of next-generation CAR-T cell therapy.

Results

CARs increase T-cell proliferation and reshape metabolome

A key step in CAR-T cell therapy development is to eliminate inefficient CAR candidates before nominating clinical candidates. Here, we sought to identify metabolic phenotypes that could serve as telltale signs of CAR-T cell efficacy.

We generated a panel that consists of one (FMC63-based) anti-CD19 CAR and five anti-CD20 CARs as well as a negative control expressing the truncated epidermal growth factor receptor (EGFRt), which serves as a non-CAR transduction marker (Fig. 1a). The anti-CD20 CARs were constructed with scFv domains derived from the antibodies Leu16,

rituximab^{24,25}, and their hybrid RFR-LCDR (Fig. 1b), whose dissociation constants (K_D) for CD20 were 138, 118, and 84 nM, respectively²². Furthermore, we generated rituximab.AA and RFR-LCDR.AA CARs, which contain insertions of two alanine residues between the transmembrane and cytoplasmic signaling domains of the CAR. The RFR-LCDR and alanine-inserted CARs have been shown to improve CAR-T cell functionality²². The anti-CD19 CAR utilizes a 12-aa IgG4 hinge as extracellular spacer, whereas the anti-CD20 CARs utilizes a 229-aa IgG4 hinge-CH2-CH3 spacer. The spacers were optimized for the respective target antigens and chosen for clinical relevance²⁰. All CAR proteins contained the identical CD28 transmembrane and cytoplasmic domains and CD3 ζ cytoplasmic domain for intracellular signaling. Thus, the CARs in our panel differed only in non-signaling residues.

We evaluated the impact of CAR protein expression on CAR-T cell expansion and metabolism during *ex vivo* culture (Fig. 1c). CAR-T cells maintained their cell numbers and viability for at least 20 days *ex vivo*, indicating their health and suitability for metabolic profiling during this period (Extended Data Fig. 1a,b). CAR surface expression in T cells were similar across the panel (Extended Data Fig. 1c). Consistent with most CAR-T cell products used clinically, the CAR-T cells used in our studies contained a mixture of CD4⁺ and CD8⁺ at their naturally occurring ratios, which varied from donor to donor, but CAR expression altered T-cell populations similarly, increasing effector memory subtype while decreasing naïve cells (Extended Data Fig. 1d and Supplementary Table 1). To assess how different scFvs affect CAR-T cell proliferation, we counted cells each day for up to three days in RPMI media supplemented with 10% dialyzed FBS (dFBS). The use of dFBS disambiguates the metabolic effects of small molecules found in FBS. A mixed-effects model was used to discern the effects of CARs on the proliferation of T cells originating from different donors. All four rituximab-based (i.e., rituximab, rituximab.AA, RFR-LCDR, and RFR-LCDR.AA) CAR-T cells grew significantly faster than EGFRt control T cells, while CD19 and Leu16 CAR-T cells grew at similar rates as the controls (Fig. 1d, Extended Data Fig. 1e, and Supplementary Table 2).

To investigate whether the disparate growth effects correlated with metabolism, we measured intracellular metabolite levels of CAR-T cells by LC-MS. T cells displayed metabolomic profiles that differed with CAR proteins expressed (Extended Data Fig. 2). Focusing on central carbon metabolism (Fig. 1e and Supplementary Table 3), we observed that all four rituximab-based CAR-T cells had significantly elevated levels of fructose-1,6-bisphosphate (FBP) compared with EGFRt control T cells, reflecting enhanced glycolytic flux²⁶ (Extended Data Fig. 3a). Rituximab CAR-T cells also possessed higher levels of the TCA cycle intermediates citrate, α -ketoglutarate (α KG), and malate than EGFRt control T cells (Extended Data Fig. 3b). While all CAR-T cells maintained redox homeostasis, rituximab CAR-T cells had a lower ATP/ADP ratio compared with EGFRt cells (Extended Data Fig. 3c). These observations suggested CAR-dependent reprogramming of T-cell energy metabolism.

CAR expression activates aerobic glycolysis

A primary goal of cellular metabolism is to produce energy and biochemical building blocks. Our observation of increased proliferation in the four rituximab-based CAR-T cells implied increased metabolic fluxes. We first compared glycolytic fluxes among CAR-T cells by measuring their glucose uptake rates and lactate secretion rates (Fig. 2a). Glucose uptake rates doubled in rituximab and rituximab.AA CAR-T cells compared with EGFRt control T cells (Fig. 2b). Interestingly, Leu16 and rituximab CARs with 92% scFv sequence identity displayed disparate glucose uptake (Supplementary Tables 4 and 5). All four rituximab-based CAR-T cells displayed stronger fermentative glycolysis, converting higher fractions of glucose into lactate, compared with EGFRt control T cells (Fig. 2b and Extended Data Fig. 3d).

To probe how CAR-T cells utilized glucose, we traced [1,2-¹³C₂]glucose through glycolysis and the PPP (Fig. 2c). Glucose-6-phosphate (G6P) is the branching point between glycolysis and the oxidative pentose phosphate pathway (oxPPP), which generates NADPH and the ribose ring of nucleotides. Glycolytic intermediates fructose-6-phosphate (F6P) and glyceraldehyde-3-phosphate (GAP) participate reversibly in the non-oxidative PPP (non-oxPPP). When metabolized through the oxPPP, [1,2-¹³C₂]glucose uniquely generates singly labeled (M+1) pentose phosphate and triose phosphate, whereas glycolysis generates doubly labeled (M+2) triose phosphate. Thus, the ratio of M+1 to M+2 lactate indicates the oxPPP flux relative to glycolytic flux. Across CAR-T cells, we observed lower fractions of glucose flux being diverted to oxPPP compared with EGFRt control T cells (Fig. 2d).

We examined the contribution of oxPPP versus non-oxPPP to pentose phosphate, a precursor to nucleic acid synthesis. Depending on its synthesis route (oxPPP vs. non-oxPPP), pentose phosphate becomes M+1 or M+2 labeled on its first two carbons (Fig. 2e). The reversibility of the transketolase reaction can add two ¹³C labeling in the last three positions of pentose, generating M+3 and M+4 pentose phosphate, respectively. The odd-to-even ratio of pentose phosphate labeling showed that CAR-T cells sourced the ribose ring of nucleotides similarly (Fig. 2f). Taken together, these observations suggested that CAR-T cells maintain low oxPPP fluxes relative to glycolysis, and rituximab-based CARs turn on aerobic glycolysis in T cells.

CAR expression upshifts nutrient utilization

Cell proliferation is linked to amino acid uptake as proteins account for the majority of cell biomass²⁷. We measured the rates of amino acid uptake across CAR-T cells by extracellular metabolomics. All CAR-T cells showed overall faster nutrient uptake than EGFRt control T cells, with rituximab and rituximab.AA CAR-T cells increasing uptake the most (Fig. 3a). All T-cell variants consumed glutamine the fastest among all amino acids (Supplementary Table 6). Amino acids influence T-cell activation, effector function, and fate²⁸. T-cell activation initially depends on extracellular asparagine although prolonged activation upregulates asparagine synthetase and decreases asparagine dependence²⁹. Elevated arginine uptake is linked to superior T-cell survival and anti-tumor activity⁶. Rituximab and rituximab.AA CAR-T cells showed the highest increase in glutamine and arginine uptake along with decreased asparagine dependence (Fig. 3a), suggesting that they may be poised

for rapid activation and initiation of anti-tumor activity. The altered amino acid uptake profiles point to different abilities of CAR-T cell variants to activate and fight tumors.

All but Leu16 CAR-T cells secreted glutamate faster than EGFRt control T cells (Fig. 3b). The increased glutamate secretion corresponded to as much as 15% of glutamine uptake being “wasted” by CAR-T cells instead of being used for protein synthesis or energy generation (Extended Data Fig. 3e). Despite the dependence of T cells on extracellular alanine for protein synthesis³⁰, rituximab and rituximab.AA CAR-T cells also secreted alanine at significantly elevated rates compared with control cells (Fig. 3c). To investigate whether extracellular alanine would deter alanine secretion, we cultured cells in RPMI-1640 medium supplemented with 10% FBS, which resulted in a final alanine concentration of ~150 μ M (ref.³⁰). While anti-CD19 and Leu16 anti-CD20 CAR-T cells as well as EGFRt control T cells consumed alanine, all four rituximab-based CAR-T cells still secreted alanine at significant rates (Extended Data Fig. 3f). The uptake and secretion measurements across CAR-T cell variants pointed to CAR-dependent nutrient utilization.

We next examined the TCA cycle, the central hub of various nutrient metabolism³¹, by tracing [U-¹³C₆]glucose and [U-¹³C₅]glutamine (Extended Data Fig. 4a,b and Supplementary Tables 7 and 8). Since the effect of alanine insertion (.AA) on nutrient uptake and byproduct secretion was minor compared with that of scFv choices, we henceforth focused on scFv-specific metabolic differences. The ¹³C-labeling fractions of the TCA cycle intermediates from [U-¹³C₆]glucose revealed that glucose contributed fewer carbons to α KG, which is the first carbonaceous metabolite in glutaminolysis, in rituximab and RFR-LCDR CAR-T cells than in EGFRt T cells and other CAR-T cells (Extended Data Fig. 4c). Glutamine contributions to the TCA cycle across CAR-T cells varied to a lesser extent, but α KG gained significantly more ¹³C from [U-¹³C₅]glutamine in rituximab CAR-T cells than in EGFRt T cells (Extended Data Fig. 4d). Glutamine contributed more to the TCA cycle metabolites downstream of citrate than glucose did on a carbon basis (Extended Data Fig. 4e). The flipped carbon contributions between citrate and α KG suggested substantial diversion of citrate away from the TCA cycle toward fatty acid synthesis.

When comparing each CAR-T cell variant against EGFRt control T cells, rituximab CAR-T cells displayed the greatest departure in both ¹³C tracing and transport fluxes (Fig. 2b, Fig. 3a–c, and Extended Data Fig. 4). We thus set out to quantify central carbon metabolism fluxes in these two T-cell variants. For ¹³C-based metabolic flux analysis (¹³C-MFA), we developed a carbon-balanced flux model of central carbon metabolism and glutaminolysis and computed flux values that best fit experimental data for nutrient uptake, byproduct secretion, and ¹³C-labeling patterns in cells that were fed [1,2-¹³C₂]glucose, [U-¹³C₆]glucose, or [U-¹³C₅]glutamine (Supplementary Tables 9–11). The main intracellular flux in both T-cell variants was glycolysis. Rituximab CAR-T cells extensively utilized aerobic glycolysis (Fig. 3d). Compared with EGFRt control T cells, rituximab CAR-T cells lowered the anaplerotic flux through pyruvate carboxylase (PC) to compensate for the faster amino acid uptake and increased the channeling of the acetyl group of acetyl-CoA into fatty acid synthesis rather than oxidizing it. The differences in the TCA cycle turning and the PPP were muted (Fig. 3d).

Rituximab-based CAR-T cells increase nucleotide turnover

We sought to understand the effect of increased amino acid uptake on the nitrogen metabolism of CAR-T cells. Since glutamine was the greatest source of nitrogen for T cells (Supplementary Table 6), we cultured CAR-T cells in medium containing 50% [γ - ^{15}N]glutamine and traced its heavy nitrogen by LC-MS. The possible fates of nitrogen on the amide of glutamine include proteins, asparagine, nucleotides, hexosamines, and ammonia (Fig. 4a). The ^{15}N from [γ - ^{15}N]glutamine was incorporated into both purines and pyrimidines with up to one ^{15}N (M+1) in UTP, two ^{15}N (M+2) in CTP and ATP, and three ^{15}N (M+3) in GTP (Fig. 4b). In the same duration (72 hours) of [γ - ^{15}N]glutamine feeding, nucleotides in rituximab and RFR-LCDR CAR-T cells gained more ^{15}N than EGFRt T cells (Fig. 4c, Extended Data Fig. 5a, and Supplementary Table 12). Consistent with the faster turnover of nucleotides in these two CAR-T cells, in the same duration (48 hours) of [1,2- $^{13}\text{C}_2$]glucose feeding, the ribose rings of their nucleotides gained significantly more ^{13}C labeling than in EGFRt T cells (Fig. 4d, Extended Data Fig. 5b, and Supplementary Table 13). It has been shown that effector T cells have limited pyrimidine biosynthesis capacity, making them sensitive to pyrimidine starvation³². Thus, the elevated pyrimidine biosynthesis capacity in rituximab and RFR-LCDR CAR-T cells may support effector cell formation and preservation.

Rituximab and RFR-LCDR CAR-T cells also increased the turnover of hexosamine biosynthesis pathway intermediates N-acetylglucosamine phosphate (GlcNAc-1/6P) and UDP-N-acetylglucosamine (UDP-GlcNAc) compared with EGFRt control T cells (Fig. 4e and Supplementary Table 13). These metabolites may indicate the cellular nutritional status³³ as UDP-GlcNAc synthesis requires carbohydrates, glutamine nitrogen, an acetyl group, and a pyrimidine. UDP-GlcNAc is a nucleotide sugar that is a donor substrate for protein and lipid glycosylation³⁴. UDP-GlcNAc is also used for O-GlcNAcylation, which regulates cellular processes such as transcription, protein ubiquitination, and cell cycle³⁵. During early stages of activation, T cells have been shown to increase flux towards O-GlcNAcylation as a regulatory modification to control protein function by increasing the levels of UDP-GlcNAc³⁶. These observations suggested that the increased nutrient uptake by rituximab and RFR-LCDR CAR-T cells may entail systems-level alteration of biochemical networks beyond metabolism.

Rituximab CAR-T cells operate nitrogen overflow metabolism

Glutamine passes on nitrogen to glutamate and ammonia via the glutaminase reaction (Fig. 4a). Consistent with their increased glutamine uptake and glutamate secretion (Fig. 3a,b), rituximab and RFR-LCDR CAR-T cells secreted ammonia faster than EGFRt control T cells (Fig. 5a). To test whether ammonia generation is reversible (i.e., it can be incorporated back into cellular metabolism), we added $^{15}\text{NH}_4\text{Cl}$ to the culture media and traced ^{15}N (Extended Data Fig. 6a). Glutamate dehydrogenase and carbamoyl phosphate synthetase can take ammonia as a substrate to form glutamate and carbamoyl phosphate (as well as downstream amino acids, pyrimidines, and urea). While these metabolites were minimally ^{15}N -labeled, we observed small increases in ^{15}N labeling of glutamate in anti-CD19 and rituximab-based CAR-T cells (Extended Data Fig. 6b) and a decrease in ^{15}N labeling of carbamoyl phosphate in rituximab CAR-T cells compared with EGFRt control T cells (Extended Data Fig. 6c).

The presence of ^{15}N in glutamine was more substantial than in glutamate, albeit still low. We observed significantly lower ^{15}N labeling in glutamine in anti-CD19 and rituximab-based CAR-T cells, which indicated their lower glutamine synthetase activity, than in EGFRt control T cells (Extended Data Fig. 6d). These results suggested that while CARs affect both the production and the (limited) reincorporation of ammonia by T cells, T cells do not utilize ammonia as a meaningful nitrogen source.

To account for the increased amino acid uptake in rituximab and RFR-LCDR CAR-T cells, we sought to identify other secreted nitrogenous products (Fig. 5b). Providing cells with 50% [γ - ^{15}N]glutamine and measuring their labeling over multiple days revealed that rituximab CAR-T cells secreted ^{15}N -labeled uracil, thymine, and xanthine the fastest among all the T cells tested (Fig. 5c,d, Extended Data Fig. 6e, and Supplementary Table 14). Taken together, CAR-T cells with highly upregulated amino acid uptake operate nitrogen overflow metabolism, secreting ammonia, alanine, glutamate, and nucleobases. On one hand, the inefficient nitrogen metabolism found in such hypermetabolic CAR-T cells may portend poor anti-tumor efficacy, especially if cancer cells also secrete nitrogenous byproducts³⁷. On the other hand, the excess pyrimidine biosynthesis capacity may serve as a reserve flux to support differentiation and proliferation on demand in rituximab-based CAR-T cells³².

To discern the effects of secretion products that may accumulate in the tumor microenvironment^{38–40}, we treated cells with 300 μM alanine, 800 μM ammonia, 30 mM lactate, or 800 μM ammonia and 30 mM lactate. Extracellular alanine exerted CAR-dependent positive and negative effects on proliferation rates (Fig. 5e). Those that absorbed alanine (EGFRt T cells and anti-CD19 and Leu16 anti-CD20 CAR-T cells; Extended Data Fig. 3f) proliferated faster with alanine supplementation while the opposite was true for RFR-LCDR CAR-T cells. High ammonia levels have been shown to induce T-cell metabolic reprogramming, increase exhaustion, and decrease proliferation³⁷, and extracellular lactate has been demonstrated to suppress T-cell proliferation in a concentration-dependent manner⁴¹. In line with these findings, the addition of ammonia and/or lactate led to slower proliferation of rituximab and RFR-LCDR CAR-T cells, the same ones that elevated the secretion of ammonia and lactate (Fig. 5e). Thus, hypermetabolic rituximab CAR-T cells may increasingly self-limit proliferation in the tumor microenvironment due to the accumulation of and low tolerance to secreted products. Our observations suggested that the impact of the extracellular environment on T-cell proliferation is dependent on their metabolic states.

To understand how the *in vitro* fitness translates to the *in vivo* efficacy of CAR-T cells, NOD/SCID/IL-2R γ^{null} (NSG) mice were intravenously injected with CD19⁺CD20⁺ Raji or Ramos lymphoma cells, and we observed how the subsequent injection of (CAR-)T cells would affect animal survival. Ramos cells grew faster than Raji cells *in vitro* (Extended Data Fig. 6f), yet Raji cells displayed faster nutrient uptake and waste secretion rates (Extended Data Fig. 6g and Supplementary Table 15). Against Raji cells, RFR-LCDR CAR-T cells have been shown to perform the best among all anti-CD19 and anti-CD20 CAR-T cells tested, clearing both primary and secondary tumor challenges²². However, the advantage of RFR-LCDR cells disappeared in the Ramos tumor model (Extended Data Fig. 6h).

To understand why the anti-tumor efficacy of different CAR-T cells varied depending on the tumor model, we developed an overflow metabolism score for CAR-T cells and a metabolic compatibility score for pairs of CAR-T cells and cancer cells (see Supplementary Note 1). Overflow metabolism score represents the extent of byproduct secretion fluxes within our CAR-T cell panel. Metabolic compatibility score represents how dissimilar a pair of cell types are in terms of nutrient uptake and byproduct secretion fluxes; for example, if both cell types secreted (or consumed) a metabolite, compatibility is deemed low, whereas if one cell type consumed and the other secreted it, compatibility is deemed high. We observed that the longest surviving groups generally had a metabolic compatibility score of 0.4 or higher and an overflow metabolism score of 0.2 or higher (Fig. 5f). These results point to dual metabolic objectives in engineering CAR-T cells for superior antitumor efficacy of CAR-T cells: compatible and modest metabolic fluxes that enable T cells to endure in and adapt to the tumor microenvironment.

Disparate CARs may render T cells similarly hypermetabolic

With rituximab CAR elevating carbon and nitrogen metabolism of T cells the most among the six anti-CD20 and anti-CD19 CARs evaluated, we were curious how it would compare against a 14g2a-based anti-GD2 CAR, which has been reported to activate T cells by ligand-independent aggregation of CAR proteins mediated through the FR of the scFv²³. We constructed the anti-GD2 CAR identically to the anti-CD20 CARs except for the scFv domain, which was derived from the 14g2a antibody (Fig. 6a). We compared the metabolic activities of rituximab anti-CD20 CAR-T cells and 14g2a anti-GD2 CAR-T cells by measuring their nutrient uptake and byproduct secretion rates as well as the isotope labeling patterns of intracellular metabolites. Transport fluxes showed some significant differences between the two CAR-T cell variants, but as a whole, their metabolic fluxes were near the line of unity (Fig. 6b). The two divergent CAR-T cell variants also exhibited similar metabolite labeling patterns upon feeding [U-¹³C₆]glucose, [U-¹³C₅¹⁵N₂]glutamine, or [γ -¹⁵N]glutamine (Fig. 6c). Comparing rituximab and 14g2a CAR-T cells, the total distances from the individual fluxes and labeling data points to the line of unity were 1.85 and 1.61, respectively, the smallest among all pair-wise comparisons with 14g2a CAR-T cells (Extended Data Fig. 7a,b). The resemblance between rituximab and 14g2a CAR-T cells extended to the secretion of nucleobases (Extended Data Fig. 7c). Despite their sequence identity being only 64% (Supplementary Tables 4 and 5), 14g2a anti-GD2 CAR-T cells were similarly hypermetabolic as rituximab anti-CD20 CAR-T cells.

Metabolism was reprogrammed across the seven CAR-T cell variants to different extents. While the effect of extracellular ligand-binding domains (i.e., scFvs) was dominant, modifying the intracellular non-signaling component (i.e., two-alanine insertions) exerted small but measurable effects. Rituximab and rituximab.AA CAR-T cells differed in thymine and xanthine secretion (Extended Data Fig. 7d). We also observed small but significant differences in nucleotide and hexosamine biosynthesis with and without alanine insertions (Extended Data Fig. 8). Our results showed that reprogramming of the basal metabolism of CAR-T cells is prevalent with modifications in the non-signaling residues of the CAR, but the nature of the metabolic reprogramming defies easy prediction. While CARs that have similar sequences and target the same antigen (e.g., Leu16, rituximab, and RFR-LCDR) can

differentially reprogram T-cell metabolism, two CARs that have low sequence identity and target different antigens (e.g., rituximab and 14g2a) do not necessarily result in disparate metabolism.

CARs alter key signaling and metabolic steps to control flux

We set out to gain mechanistic insights into the observed metabolic rewiring in CAR-T cells. One of the primary factors influencing metabolic fluxes is the enzyme activity at the rate-determining steps. Experimental and theoretical studies have suggested the tendency of reactions at the beginning, the end, and the “irreversible” (i.e., thermodynamically forward-driven) steps of a pathway to be rate-determining^{26,42,43}. Bulk RNA sequencing (RNA-seq) revealed that in unstimulated rituximab anti-CD20 and anti-GD2 CAR-T cells, the transcripts corresponding to the key control steps of glycolysis, nucleotide biosynthesis, and glutaminolysis (but not the TCA cycle or the PPP) were higher compared with other T cells (Fig. 6d, Extended Data Fig. 9, and Supplementary Table 16). The disparate gene expression may be due to unintended phosphorylation of CAR signaling molecule CD3 ζ and/or costimulation of CD28 that initiate signaling cascades such as mTOR, GSK3, and GRB2-SOS pathways⁴⁴.

To identify which unintended phosphorylation event initiates signaling cascades, we generated three mutants of the hypermetabolic rituximab CAR (rituximab.28–3z) that are incapable of tyrosine phosphorylation by introducing P208/211/212A and Y191F substitutions in CD28^{45,46} and/or Y-to-F substitutions in the three immunoreceptor tyrosine-based activation motifs (ITAMs) of CD3 ζ ⁴⁷: rituximab.28^{mt}-3z, rituximab.28–3z^{mt}, and rituximab.28^{mt}-3z^{mt} CAR-T cells (Fig. 6e). Non-mutated and rituximab.28^{mt}-3z CAR-T cells showed significantly increased proliferation rates (Fig. 6f and Supplementary Table 17), metabolic rates (Fig. 6g and Supplementary Table 18), and T-cell activation- and exhaustion-marker expression (Extended Data Fig. 10a and Supplementary Table 19) compared to the EGFRt control T cells. In contrast, rituximab.28–3z^{mt} and rituximab.28^{mt}-3z^{mt} CAR-T cells exhibited similar behavior as the control and Leu16 CAR-T cells. Thus, CD3 ζ signaling, rather than CD28 signaling, was the major contributor to unintended phosphorylation. Analysis of phosphopeptides using LC-MS corroborated that CD3 ζ but not CD28 was phosphorylated and revealed that the higher phosphorylation of the second ITAM (ITAM2) of CD3 ζ corresponded to hypermetabolic CAR-T cells (Extended Data Fig. 10b and Supplementary Table 20).

Positively charged patches (PCPs) on the surface of scFvs have been reported to affect CAR protein conformation and membrane transport⁴⁸, and might serve to explain why the same signaling domains would be differentially activated in different CARs. The potential interaction between PCPs and negatively charged membrane molecules⁴⁸ may trigger activation signals, akin to how the self-aggregation of anti-GD2 scFv leads to ligand-independent activation²³. We observed that the anti-GD2 and rituximab anti-CD20 scFvs had large PCPs as well as the highest net positive charge in our panel (Extended Data Fig. 10c and Supplementary Table 21). Furthermore, we found that although CAR expression in general resulted in upregulation of several markers associated with T-cell activation and

exhaustion, high CD137 and LAG3 expression particularly coincided with hypermetabolism in CAR-T cells (Extended Data Fig. 10d and Supplementary Table 22).

Discussion

CARs enable T cells to recognize and attack target cells expressing a cognate ligand. The most successful CAR-T cell therapies to date target hematological malignancies that express CD19 or BCMA⁴⁹. Expanding the applicability of CAR-T cell therapy to other diseases entails tuning of antigen specificity and affinity as well as intracellular signaling. Development of new CARs involves the combinatorial assembly of peptide domains responsible for these parameters, expressing CAR proteins in T cells, and identifying promising CAR designs through screening in tissue cultures and animal models. Understanding how the domains of CAR proteins impact the intracellular biochemical networks of T cells would streamline this process by providing an in-depth look at T-cell physiology and reducing trial and error.

Metabolism is a network of biochemical reactions that supports T-cell proliferation and anti-cancer activity by supplying cellular energy and biochemical building blocks. Different intracellular co-stimulatory and signaling domains can differentially modulate CAR-T cells' metabolism and efficacy. CARs have been classified according to modifications in their intracellular signaling domains. First-generation CARs consist of the CD3 ζ signaling domain alone, and second- and third-generation CARs include the addition of one or two costimulatory domains (e.g., 4-1BB and CD28)⁵⁰. A study comparing T cells expressing 4-1BB- versus CD28-containing CARs has reported that 4-1BB CARs promote mitochondria-rich memory T cells with superior metabolic capacity, antitumor activity, and persistence; in contrast, CD28 CARs are more likely to yield short-lived effector T cells that rely on heightened glycolysis, a phenotype that could be useful in contexts where long-term CAR effects are intolerable⁵¹. CAR-T cells that simultaneously target two tumor-associated antigens while providing both CD28 and 4-1BB costimulation promote both glycolysis and mitochondrial respiration⁵². T-cell metabolism and fate are clearly influenced by the selection of intracellular signaling domains. CAR ectodomains (e.g., extracellular spacers) have also been shown to affect the anti-tumor efficacy of CAR-T cells despite their lack of intrinsic signaling function^{22,53}. However, the effect of the scFv and non-signaling portions of CARs on T-cell metabolism remained underexplored. The present work sheds light on systems-level metabolic reprogramming of CAR-T cells that accompanies the modification of the extracellular scFv and intracellular non-signaling portions.

We quantified cell proliferation and mapped metabolic pathway utilization across seven CAR-T cell variants that only differed in non-signaling portions of CAR proteins. We varied the extracellular components with five different scFvs targeting three different antigens (CD19, CD20, and GD2) and, for two of the anti-CD20 CARs, we inserted two alanine residues between the transmembrane and intracellular domains²². Our work highlighted three important lessons: *i*) mere expression of CARs can increase T-cell proliferation and metabolic activity; *ii*) replacement of non-signaling components of CARs differentially rewires metabolism; and *iii*) CARs with similar scFv sequences can have disparate metabolic profiles while CARs with disparate scFv sequences can lead to similar

hypermetabolism in T cells. Hypermetabolic CAR-T cells operate overflow metabolism, secreting lactate, alanine, glutamate, ammonia, and nucleobases disproportionately fast. The accumulation of secreted metabolites affects T-cell proliferation in a metabolic-state-dependent manner. Thus, while CARs reprogram T-cell metabolism rather unpredictably, once we profile CAR-T cell metabolism, we can predict the environments in which CAR-T cells thrive.

All seven CAR-T cell variants increased overall nutrient uptake, and a subset of them also increased proliferation rates. The choice of scFv affected metabolic fluxes to a larger extent than alanine insertion in the intracellular non-signaling portion of CAR. Unexpectedly, we saw substantial alanine production by the four rituximab-based (rituximab, RFR-LCDR, rituximab.AA, and RFR-LCDR.AA) CAR-T cells. This observation was in contrast to other anti-CD20 (Leu16) CAR-T cells, anti-CD19 CAR-T cells, and EGFRt control T cells, which consumed alanine, and activated T cells, which have been shown to take in extracellular alanine for protein synthesis³⁰. These anomalies hinted at a potential metabolic imbalance in rituximab-based CAR-T cells: cells consumed more nutrients than necessary for biomass, cytokine, and energy generation.

Lactate secretion is the epitome of overflow metabolism, in which cells secrete seemingly useful molecules⁵⁴. Rituximab CAR-T cells, which consumed glucose and amino acids the fastest among the CAR-T cells tested, secreted excess carbons the fastest through lactate. What about the excess nitrogen? In addition to alanine, we observed increased secretion of glutamate, ammonia, and nucleobases by rituximab CAR-T cells. While the accumulation of ammonia has been shown to have detrimental effects on T cells³⁷, how the other nitrogenous molecule buildup affects T cells remains to be seen. The inefficient nitrogen metabolism may undermine the hyperactive CAR-T cells' ability to proliferate and attack cancer cells in a tumor microenvironment containing high levels of nitrogen waste⁵⁵.

On a fundamental level, our observations showed that the scFv domain has impacts on CAR and CAR-T cells beyond antigen specificity. Although we found that similar non-signaling components of CARs differentially reprogram metabolism, different CARs do not necessarily result in different T-cell metabolism. Rituximab anti-CD20 CAR-T cells and 14g2a anti-GD2 CAR-T cells showed similarly hyperactive metabolism despite the low sequence identity. The varying expression levels, structural and electrostatic properties, and dissociation constants of CAR may collectively contribute to the observed metabolic reprogramming. Ligand-independent signaling, a phenomenon commonly referred to as tonic signaling, through the phosphorylation of ITAM2 of CD3 ζ ⁵⁶ and the upregulation of metabolic genes at the key control steps capable of exerting changes in metabolic fluxes were observed as intermediate steps in reprogramming CAR-T cell metabolism.

Overall, our observations imply that simply swapping out one scFv for another may entail systems-level rewiring of cellular biochemical networks even if the rest of the CAR protein, including all signaling domains, remains the same. Despite the apparent modularity of the peptide domains of CARs and the widespread practice of combinatorial assembly of the domains to develop new CAR proteins⁵, a holistic assessment of CAR proteins is warranted

to learn how different domains within a given CAR molecule interact and how CAR proteins interact with each other and other cellular components.

A limitation of our study was a batch effect that is attributable to both donor-intrinsic differences (e.g., genetic factors, age, sex, diet, CD4⁺-to-CD8⁺ T-cell ratio, etc.) and batch-to-batch differences in CAR-T cell generation and cellular metabolite extraction. To account for donor-to-donor variability, we used mixed-effects models. The measurement of the isotope labeling fractions of intracellular metabolites and extracellular metabolite levels obviates the concerns associated with cellular metabolite extraction. An improved understanding and control of underlying variables that govern T-cell metabolism will enable more sensitive detection of CAR-dependent metabolic reprogramming.

The different metabolic rates and pathway usage across the CAR-T cell variants suggested that different CAR-T cells may function optimally in different nutrient environments¹², and that the optimal CAR construct for a given tumor may be dependent on the specific tumor microenvironment. CAR-T cells with fast basal metabolic activity could be poised to unleash rapid initial anti-cancer cytotoxicity by swiftly ramping up the supply of necessary cellular machinery and energy. On the other hand, less metabolically active cells may be less effective at killing cancer cells initially but may sustain their effectiveness longer by having a more adaptive metabolism. While many factors influence the efficacy of CAR-T cell therapy, the present work identifies modest overflow metabolism of CAR-T cells and metabolic compatibility in the tumor microenvironment as dual metabolic objectives for the development of efficacious CAR-T cell therapy. With increasing knowledge of the metabolism of clinically successful (and unsuccessful) CAR-T cells, metabolic reprogramming would serve as an important prognostic marker for streamlined CAR design, and metabolic engineering should be an integral task in successful CAR-T cell therapy development.

Materials and Methods

Construction of scFvs and CARs

The anti-CD19 scFv was derived from FMC63 monoclonal antibody (mAb)⁵⁷. The plasmid encoding the scFv sequence of rituximab was provided by Dr. Anna M. Wu of UCLA and City of Hope⁵⁸. The plasmid encoding the scFv derived from Leu16 mAb was provided by Dr. Michael C. Jensen of the Seattle Children's Research Institute⁵⁹. AbYsis was used to obtain the V_L and V_H sequences of the anti-GD2 scFv from the 14g2a mAb (Protein Data Bank entry 4TUJ). Anti-CD20 CARs were constructed by fusing an scFv (in V_L-V_H orientation), an extracellular IgG4 hinge-CH2-CH3 spacer containing L235E N297Q mutations⁵³, the CD28 transmembrane and cytoplasmic domains, the CD3ζ cytoplasmic domain, a T2A self-cleaving peptide sequence, and a truncated epidermal growth factor receptor (EGFRt) with the MSCV backbone. The 14g2a-based anti-GD2 CAR was constructed identically to the anti-CD20 CARs except for the scFv (in V_H-V_L orientation for anti-GD2). The anti-CD19 CAR was constructed with the FMC63-based scFv (in V_L-V_H orientation), an IgG4 hinge extracellular spacer, and the identical transmembrane and cytoplasmic domains as the anti-CD20 and anti-GD2 CARs. The IgG4 hinge for the CD19 CAR was based on previous studies showing different structural requirements for

optimal CD19 and CD20 antigen targeting⁵³. CARs containing two alanine residues were created using DNA sequences inserted between the CD28 transmembrane and cytoplasmic domains using isothermal assembly. RFR-LCDR and RFR-LCDR.AA anti-CD20 CARs were constructed as gene block fragments (Integrated DNA Technologies) and assembled using digestion-ligation with MreI and BstBI. The anti-CD20 rituximab.28^{mt}-3z CAR had P208/211/212A and Y191F substitutions in the CD28⁴⁵ cytoplasmic domain. The anti-CD20 rituximab.28-3z^{mt} CAR had Y-to-F substitutions in the three immunoreceptor tyrosine-based activation motifs (ITAMs) of CD3 ζ ⁴⁷. The anti-CD20 rituximab.28^{mt}-3z^{mt} CAR had the same substitutions in both domains. EGFRt was used as a transduction and sorting marker²². Percent identity matrix and sequence homology of scFv was determined using T-Coffee⁶⁰.

Retrovirus production and human primary CAR-T cell generation

Retrovirus was produced by transiently co-transfecting HEK293T cells with a plasmid encoding a CAR or control construct and pRD114/pHIT60 virus-packaging plasmids (courtesy of Dr. Steven Feldman of the National Cancer Institute) using linear polyethylenimine (25 kDa; Polysciences). After 48 and 72 hours, the supernatants were collected and filtered using a membrane filter (0.45 μ m). Peripheral blood mononuclear cells (PBMCs) were isolated from healthy donor blood (courtesy of the UCLA Blood and Platelet Center) by density gradient centrifugation using Ficoll-Paque PLUS (GE Healthcare). On the day of isolation, CD14⁻/CD25⁻/CD62L⁺ naïve/memory T cells were enriched by depleting CD14⁺ and CD25⁺ cells and subsequently enriching CD62L⁺ cells by using microbeads with respective specificity (Miltenyi) and magnetic-activated cell sorting (MACS; Miltenyi). The naïve/memory T cells were stimulated with CD3/CD28 Dynabeads (ThermoFisher) at a 3:1 cell-to-bead ratio for one week at a seeding density of 1×10^6 cells/mL. On the second and third days of Dynabeads stimulation, T cells were transduced with the retroviral supernatant. Five days into stimulation, T cells were washed and reseeded at 1×10^6 cells/mL to remove residual viral supernatant. Cell viability was greater than 70%. After removing Dynabeads, CAR-T cells and EGFRt control T cells were enriched from the resulting T-cell population by staining EGFRt with biotinylated cetuximab (Eli Lilly), labeling with anti-biotin microbeads (Miltenyi), and performing MACS. T cells were expanded in RPMI-1640 media supplemented with 10% heat-inactivated FBS (HI-FBS) as well as recombinant human IL-2 (50 U/mL; ThermoFisher) and IL-15 (1 ng/mL; Miltenyi). IL-15 has been shown to support T-cell expansion and protect T cells against IL-2-mediated activation-induced cell death^{61,62}. Since human primary T cell survival is impaired in the absence of cytokines, IL-2 and IL-15 were supplemented to our culture system. *Ex vivo* expansion of T cells with IL-2 and IL-15 is a widely used method and has been shown to work well in both preclinical and clinical settings^{20,22}. Cell density was maintained at $1-2 \times 10^6$ /mL throughout the CAR-T cell production and expansion process.

CAR-T cell culture conditions

At the start of experiments for metabolic profiling and proliferation measurement, each CAR-T cell variant was moved to three wells in a 12-well plate containing RPMI-1640 media supplemented with 10% dFBS, 50 U/mL IL-2, and 1 ng/mL IL-15 unless otherwise specified. Partial media change was performed by removing a third of

consumed media and adding the same volume of fresh media every 24 hours to prevent nutrient depletion. For isotope labeling experiments, CAR-T cells were cultured in media containing [1,2-¹³C₂]glucose, [U-¹³C₆]glucose, 50% [U-¹³C₅¹⁵N₂]glutamine, and/or 50% [γ -¹⁵N]glutamine (Cambridge Isotope Laboratories) for 48–72 hours. Labeled media were prepared from RPMI-1640 without glucose (Gibco) by adding the desired isotopically labeled form of glucose to a final concentration of 2 g/L and by adding the desired isotopically labeled form of glutamine to a final concentration of 0.6 g/L glutamine (resulting in 50% labeled glutamine). To trace nitrogen from ammonia, 800 μ M ¹⁵NH₄Cl was added to media. For proliferation measurement under different extracellular conditions, 300 μ M alanine, 800 μ M NH₄Cl, and/or 30 mM lactate was added to media (Supplementary Table 23).

Proliferation rate measurement

Proliferation rate was measured based on how cell numbers changed over time starting 24 hours after seeding the CAR-T cells in RPMI media supplemented with 10% dFBS. On each day, 10 μ L of the well-mixed cultures were mixed with 10 μ L of 1% flow cytometry staining buffer, and the mixture was run on a MACSQuant VYB flow cytometer, which reported total cell numbers and viability. Flow cytometry data were analyzed and gated using FlowJo (TreeStar; see Extended Data Fig. 1a for an example of gating strategy). The total cell count per well (C) was determined by accounting for the total culture volume in each well. Proliferation rate (μ) was computed using linear regression on log-transformed total per-well cell counts over time throughout the experimental periods of up to 72 hours (see Supplementary Note 2). If cell counts decreased over time, the apparent proliferation rate was set to 0 hr⁻¹:

$$\mu = \max\left(0, \frac{\Delta \ln C}{\Delta t}\right)$$

Metabolite extraction and measurement

Four hours prior to metabolite extraction, culture media was partially replaced with fresh but otherwise identical media to prevent any nutrient depletion. As metabolites turnover fast, metabolism was quenched and metabolites were extracted quickly⁶³. Cells were vacuum-filtered onto nylon membrane filters (0.45 μ m; Millipore), resting on a glass filter support. Each filter was quickly submerged cell-side down in 400 μ L of a -20°C pre-cooled extraction solvent mixture (40:40:20 HPLC-grade acetonitrile/methanol/water) in individual wells of a 6-well plate. The extraction continued for 20 minutes at -20°C. The filters were flipped cell-side up and washed thoroughly with the extraction solvent. Metabolite extracts were collected into Eppendorf tubes and centrifuged at 17,000 \times g in 4°C for 10 minutes. Supernatants were dried under nitrogen gas and reconstituted in HPLC-grade water at 10–15 μ L per 1 million cells.

Cell extracts were analyzed on a Vanquish Duo UHPLC system coupled to a Q Exactive Plus orbitrap mass spectrometer (ThermoFisher) by electrospray ionization. The order of sample injection was randomized. The LC separation was performed on a XBridge BEH Amide XP column (150 mm \times 2.1 mm, 2.5 μ m particle size, Waters, Milford, MA) using

a gradient of solvent A (95:5 water/acetonitrile with 20 mM ammonium acetate, 20 mM ammonium hydroxide, pH 9.4) and solvent B (acetonitrile)⁶⁴. Two independent LC flow paths were operated in tandem, staggered by 20 minutes. The gradient for each flow path was 0 min, 90% B; 2 min, 90% B; 3 min, 75% B; 7 min, 75% B; 8 min, 70% B; 9 min, 70% B; 10 min, 50% B; 12 min, 50% B; 13 min, 25% B; 14 min, 25% B; 16 min, 0% B; 20 min, 0% B; 23 min, 0% B; 27 min, 25% B; 30 min, 45% B; 33 min, 90% B; 40 min, 90% B. The flow rate was 150 $\mu\text{L min}^{-1}$. Injection volume was 5 μL , and autosampler and column temperatures were 4°C and 25°C, respectively. The MS operated in negative and positive ion modes with a resolution of 140,000 at mass-to-charge ratio (m/z) 200 with scan range of m/z 60–2000. Data was collected using the software Xcalibur (v4.3) (ThermoFisher). With retention times determined by authenticated standards, resulting mass spectra and chromatograms were identified and integrated using the Metabolomic Analysis and Visualization Engine (MAVEN)⁶⁵. No samples were excluded from the analyses.

Nutrient uptake and byproduct secretion measurement

Media samples were collected from each culture well every 24 hours during partial replacement of media. Glucose and lactate were measured by YSI 2950D instrument (YSI, Yellow Springs, OH) and LC-MS (with internal standards). Ammonia concentration was determined using Ammonia Assay Kit (Sigma-Aldrich AA0100) following manufactured specifications. Assay is based on ammonia reacting with α -ketoglutarate and NADPH in the presence of L-glutamate dehydrogenase to form glutamate and NADP⁺. Spectrophotometer was used to measure the absorbance at 340 nm, which declines with the oxidation of NADPH, thus revealing ammonia levels. For LC-MS measurement of nutrients and byproducts in media, HPLC-grade methanol was added to fresh and spent media samples at 80:20 methanol/sample, mixed well, and centrifuged at 17,000 \times g and 4°C for 15 minutes to precipitate proteins. Supernatants were collected and analyzed by LC-MS. Metabolite concentrations in culture media were quantified at 24, 48, and 72 hours by normalizing their ion counts to those of fresh media samples and standards with known concentrations. The order of LC-MS sample injection was randomized. As CAR-T cells did not always proliferate exponentially, uptake and secretion rates were obtained by fitting the rates to measured culture densities and extracellular metabolite concentrations (see Supplementary Notes 3 and 4).

Metabolic flux analysis

EGFRt T cells and rituximab CAR-T cells were labeled with [1,2-¹³C₂]glucose, [U-¹³C₆]glucose, or 50% [U-¹³C₅¹⁵N₂]glutamine for 48–72 hours. Metabolite labeling measurements were corrected for natural ¹³C abundance and enrichment impurity of labeled substrate. Metabolic fluxes were obtained using the model of central carbon metabolism and glutaminolysis, the elementary metabolite unit (EMU) framework⁶⁶, and mathematical optimization. Measurements of transport fluxes for glucose uptake, glutamine uptake, lactate secretion, glutamate secretion, alanine secretion, and pyruvate secretion were used to constrain the model. The ¹³C labeling patterns of intracellular metabolites were used to determine metabolic fluxes. Measured M+0 FBP labeling fraction was inexplicably high. Based on FBP aldolase reaction mechanism, which generates comparable fractions of M+0 and M+4 FBP in the reverse reaction⁶³, FBP M+0 and M+4 fractions were set equal to each

other in the [1,2-¹³C₂]glucose experiments for ¹³C-MFA. A MATLAB-scripted algorithm was used to simulate mass isotopomer distributions with fluxes as a variable and identify the flux distribution that minimized the variance-weighted sum of squared residuals (SSR) between simulated and measured isotope labeling and uptake and secretion rates:

$$\min_v \sum \left(\frac{iso_{exp} - iso(v)}{s_{iso}} \right)^2 + \sum \left(\frac{v_{exp} - v}{s_v} \right)^2$$

v is the flux vector, iso_{exp} is the experimentally observed isotope labeling, $iso(v)$ is the simulated isotope labeling, v_{exp} is the measured transport fluxes, and s denotes the standard deviation of the measured isotope labeling and fluxes. Flux distributions simulated all isotope tracer experiments simultaneously. The confidence interval (95%) of each reaction flux was obtained by searching for the minimum and the maximum flux values that increase the SSR by less than the χ^2 cutoff (1 degree of freedom) of 3.84 (ref. ⁶⁷).

RNA-seq for CAR-T cells

RNA from CAR-T cells was extracted using the Qiagen RNeasy Plus Mini kit (Qiagen). mRNA was isolated using the NEBNext Poly(A) mRNA Magnetic Isolation Module (New England BioLabs). RNA library was generated using the NEBNext Ultra II Directional RNA Library Prep Kit (New England BioLabs) and analyzed on the Illumina NovaSeq S1 platform by 50-bp paired-end sequencing at the High Throughput Sequencing core at UCLA Broad Stem Cell Research Center. The quality of the RNA-seq data was assessed using FastQC (v0.11.8)⁶⁸. The reads were processed using cutadapt (v1.18)⁶⁹ to remove low-quality reads with a quality score less than 33 and to trim adapters. The trimmed reads were mapped to the hg38 genome using Tophat2⁷⁰. The fragments corresponding to each gene were counted using the featureCounts function in the subread package (v1.6.3)⁷¹ with Ensembl 38 gene sets as references. Genes with fewer than 8 mapped reads in at least one sample were considered below the reliable detection limit and were excluded from further analysis. To normalize the read counts, the Trimmed Mean of M-values method (TMM normalization method in edgeR running on R v3.6.3) was applied, resulting in FPKM (fragments per million per kilobase) values. For rank order analysis of the 36 glycolytic genes, the binary logarithm (\log_2) of expression fold-change relative to the EGFRt control of individual glycolytic genes was ranked in descending order. The topmost upregulated GLUT (*SLC2A1* and *SLC2A3*), PFK (*PFKL*, *PFKM*, *PFKP*, *PFKFB1*, and *PFKFB3*), and MCT (*SLC16A1*, *SLC16A3*, *SLC16A7*, and *SLC16A8*) isoforms were highlighted until one isoform from each of the three key control steps of glycolysis was found²⁶.

Obtaining standard Gibbs free energy of reaction

Standard Gibbs free energy of reaction ($\Delta_r G^\circ$) were computed on eQuilibrator, which uses the component contribution method⁷². For cytosolic reactions, pH was set to 7.2, pMg was set to 1.7, and physiological ionic strength was set to 0.15 M. For mitochondrial reactions, pH was set to 8.0, pMg was set to 1.7, and physiological ionic strength was set to 0.15 M (ref. ⁶³).

Determination of positively charged patches

SWISS-MODEL, the protein structure homology-modeling server, was used to generate the 3D conformation of scFv⁷³. The protein-sol heatmap software was used to calculate net charge per surface amino acid of CAR scFvs⁷⁴. The BindUp web server was used to display the three largest positive electrostatic patches of CAR scFvs and compute PCP scores⁷⁵.

Antibody staining for flow cytometry

Transduction efficiency and CAR expression levels were measured by antibody staining of EGFRt, anti-Fc, and HA²². EGFRt was labeled with biotinylated cetuximab (Eli Lilly; biotinylated in-house), followed by PE-conjugated streptavidin (Jackson ImmunoResearch #016-110-084). Anti-Fc (Alexa Fluor 488, Jackson ImmunoResearch #709-546-098) and HA (FITC, clone GG8-1F3.3.1, Miltenyi #130-120-722) were used to measure CAR expression by surface epitope staining. Antibody staining for CD25 (APC, clone BC96, BioLegend #302610), CD69 (FITC, clone FN50, BioLegend #310904), CD137 (Brilliant Violet 421, clone 4B4-1, BioLegend #309818), CTLA-4 (APC, clone BNI3, BioLegend #369614), PD-1 (PE/Vio770, clone PD1.3.1.3, Miltenyi #130-117-698), LAG-3 (Brilliant Violet 421, clone 11C3C65, BioLegend #369314), and TIM-3 (FITC, clone F38-2E2, BioLegend #345022) was used to measure antigen-independent activation-marker and exhaustion-marker expression of CAR-T cells 17 days after Dynabead addition and 10 days after Dynabead removal. CAR-T cell subtypes were measured by antibody staining for CD45RO (VioBlue®, clone REA611, Miltenyi #130-119-620) and CD62L (APC, clone DREG56, Invitrogen #17-0629-42). Antibodies were diluted 1:100. A MACSQuant VYB flow cytometer (Miltenyi) and FlowJo software (TreeStar) were used for data acquisition and analysis.

Probing the efficacy of CAR-T cells in vivo

The animal study was performed in accordance with the protocol approved by the UCLA Institutional Animal Care and Use Committee (IACUC). The UCLA Department of Radiation and Oncology supplied six- to eight-week-old NOD/SCID/IL-2R γ ^{null} (NSG) mice²². Six mice (three female and three male) per pair of cancer and CAR-T cells were used for probing efficacy. Mice were assigned randomly to treatment groups. In the Raji xenograft study, mice were injected with 5×10^5 Raji lymphoma cells by tail-vein injection. Five to nine days later, they were treated with CAR-T cells or EGFRt control T cells via tail-vein injection (first dose was 1.35×10^6 , and second dose five days later was 1.5×10^6). Survival studies for the Raji tumor model had been performed previously (Raji-bearing mice that survived 50 days post the second CAR-T cell dose were re-challenged with 5×10^5 Raji cells)²². In the Ramos xenograft study, mice were injected with 2×10^6 Ramos lymphoma cells by tail-vein injection. Five days later, they were treated with CAR-T cells or EGFRt control T cells at a dose of 3×10^6 via tail-vein injection. Kaplan-Meier survival analysis was performed. Survival data was blinded to the operator. For each CAR-T cell and cancer cell pair, survival past EGFRt control was calculated by subtracting the average number days that control mice (treated with EGFRt T cells) survived from the number of days that mice treated with CAR-T cells survived. Mice were euthanized at humane endpoints under the American Veterinary Medical Association (AVMA) Guidelines. To minimize discomfort,

pain, distress and injury to the animals, well-trained personnel performed the procedures, and precautions were taken under the guidance of the UCLA Vivarium and Division of Laboratory Animal Medicine. No animals were excluded from the analysis. This study was not designed to find sex differences, and sex-based analyses were not performed.

Protein extraction and phosphopeptide measurement

Phosphorylation of peptides from CAR intracellular signaling domains was measured by CAR protein separation, digestion, and analysis on LC-MS/MS. CAR-T cells were washed with ice-cold PBS and lysed using RIPA lysis buffer (ThermoFisher) containing protease inhibitor (ThermoFisher) and phosphatase inhibitor (ThermoFisher) at 4°C for 30 minutes. Cell lysate was centrifuged at 17,000 x g at 4°C for 10 min to remove debris. Protein concentrations were quantified by Bradford colorimetric assay. Protein samples were separated by SDS-PAGE using Novex™ WedgeWell™ 12% Tris-Glycine Gels and SimplyBlue SafeStain (ThermoFisher). Gel bands of CAR proteins were excised and destained twice in 100 mM ammonium bicarbonate/50% acetonitrile (ACN) solution at 37°C for 30 minutes. The gel bands underwent reduction and alkylation to prepare for digestion. The gel bands were shrunk using ACN and digested overnight at 37°C with 0.01 µg/µL trypsin dissolved in 100 mM ammonium bicarbonate. The next day, peptides were extracted from gel bands by 50% ACN/5% formic acid solution with incubation at 37°C for 15 minutes, and the extraction step was repeated twice. Vacuum operator was used to evaporate liquid and samples were cleaned up with Empore StageTips. Elution from the stage-tip was dried by SpeedVac and resuspended in 3% acetonitrile with 0.1% formic acid before LC-MS/MS analysis.

Protein samples were analyzed by injecting 1.0 µg protein to an UltiMate™ 3000 Nano LC equipped with a 25-cm long, 75 µm inner diameter fused-silica capillary, packed in-house with bulk 1.9 µM ReproSil-Pur beads with 120 Å pores, using a gradient of solvent A (H₂O with 3% DMSO and 0.1% formic acid) and solvent B (ACN with 3% DMSO and 0.1% formic acid). The nanoLC gradient was 0 min, 1% B, 0.4 µL/min; 6 min, 6% B, 0.2 µL/min; 55 min, 25%, 0.2 µL/min; 63.5 min, 32%, 0.2 µL/min; 65 min, 80%, 0.2 µL/min; 67 min, 80%, 0.2 µL/min; 68 min, 1%, 0.2 µL/min; 70 min, 1%, 0.2 µL/min. The nanoLC was coupled with a Fusion Lumos orbitrap mass spectrometer (ThermoFisher). The ESI voltage was set at 2.2 kV, and the capillary temperature was set at 275°C. Full spectra (m/z range 350–2000) were acquired in profile mode with a resolution of 120,000 at m/z 200 with normalized AGC 50%. The order of LC-MS sample injection was randomized. The most abundant ions within 3 seconds of master scans were subjected to fragmentation by higher-energy collisional dissociation (HCD) with fixed collisional energy of 35%. MS/MS spectra were acquired in centroid mode with resolution 15,000 at m/z 200. The AGC target for fragment ions is set as standard with dynamic maximum injection time. Charge states 2–6 were included for tandem MS experiments. Dynamic exclusion was set at 25.0 s. Raw data was searched against full CAR protein database using the Sequest node within Proteome Discoverer (v2.5) for protein identification. The following parameters were used: precursor mass tolerance ±10 ppm, fragment mass tolerance ±0.02 Th for HCD, up to two miscleavages by semi-trypsin. Variable modifications included serine, threonine, and tyrosine phosphorylation. Cysteine carbamidomethylation was set as fixed modification.

False discovery rate was at 1.0%. Amino acid sequences of the full CARs were used to determine peptide fragments derived from CD28 and CD3 ζ . Peptide retention times and m/z were obtained from high confidence MS/MS data. Peaks corresponding to these retention time and m/z were integrated from each sample in Thermo Qual Browser. To compare the abundance of phosphorylated peptides across the CAR-T cell panel, the peak areas of phosphorylated peptides in each sample were normalized to the peak areas of the top three most abundant non-phosphorylated peptides derived from the intracellular domains of CAR within the same sample.

Statistical analysis

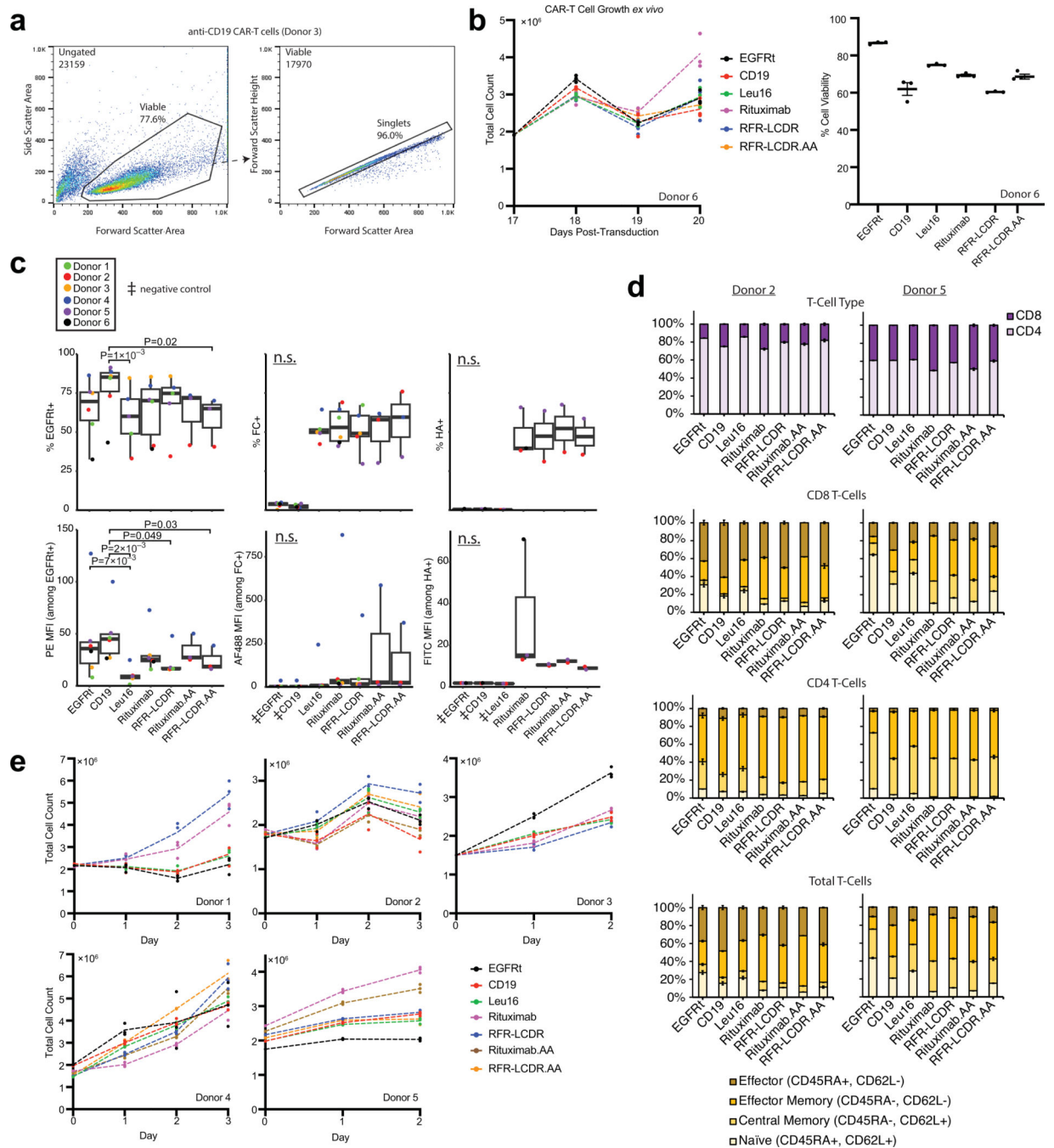
For data derived from multiple donors, statistical tests were performed using R by fitting linear mixed-effects models to the response variables. For each response variable, the linear mixed-effects models had CAR type and donor as the explanatory variables. The mixed-effects models were fit by the restricted maximum likelihood approach with CAR types as a fixed effect and donors as a random effect:

$$y = \beta_0 + CAR \beta_1 + Donor u_0 + \varepsilon$$

y represents the response variable, β_0 , the intercept term, β_1 , the fixed-effect regression coefficients for the CAR variable, u_0 , the random effect for the Donor variable, and ε , the residuals. The random effect contributed to the intercept (β_0), which was set to the reference measurement from EGFRt control T cells, but not the slopes (β_1). With the best parameters that describe the random effects and the residuals, the fitted model computed the coefficients β_1 for the fixed effects of CAR type. Statistical significance for each CAR was obtained by a t test comparing the full model with a simpler model, which contains one fewer parameter that corresponds to the CAR, using Satterthwaite's method for approximating the effective degrees of freedom.

Data distribution was assumed to be normal, but this assumption was not formally tested. No statistical methods were used to pre-determine sample sizes, but our sample sizes are similar to those reported in previous publications^{22,42}. Data collection and analysis were not performed blind to the conditions of the experiments.

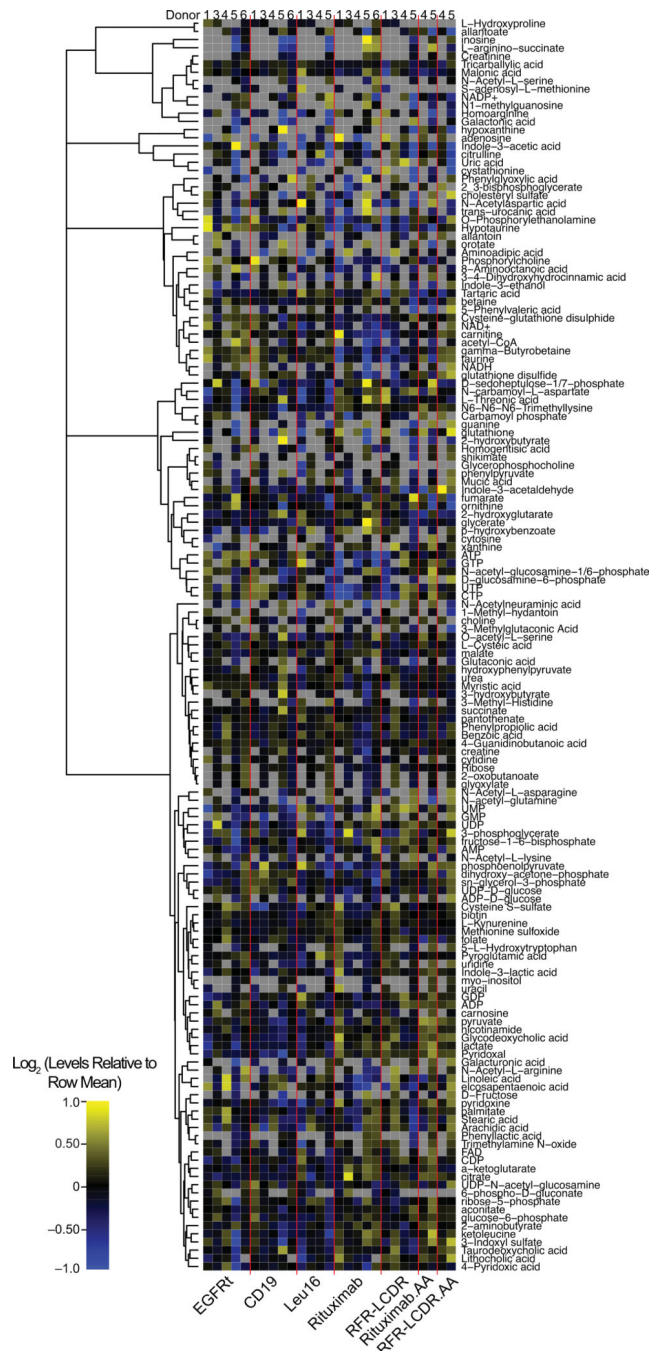
Extended Data



Extended Data Figure 1: CAR-T cell transduction efficiencies, growth, and subtypes.

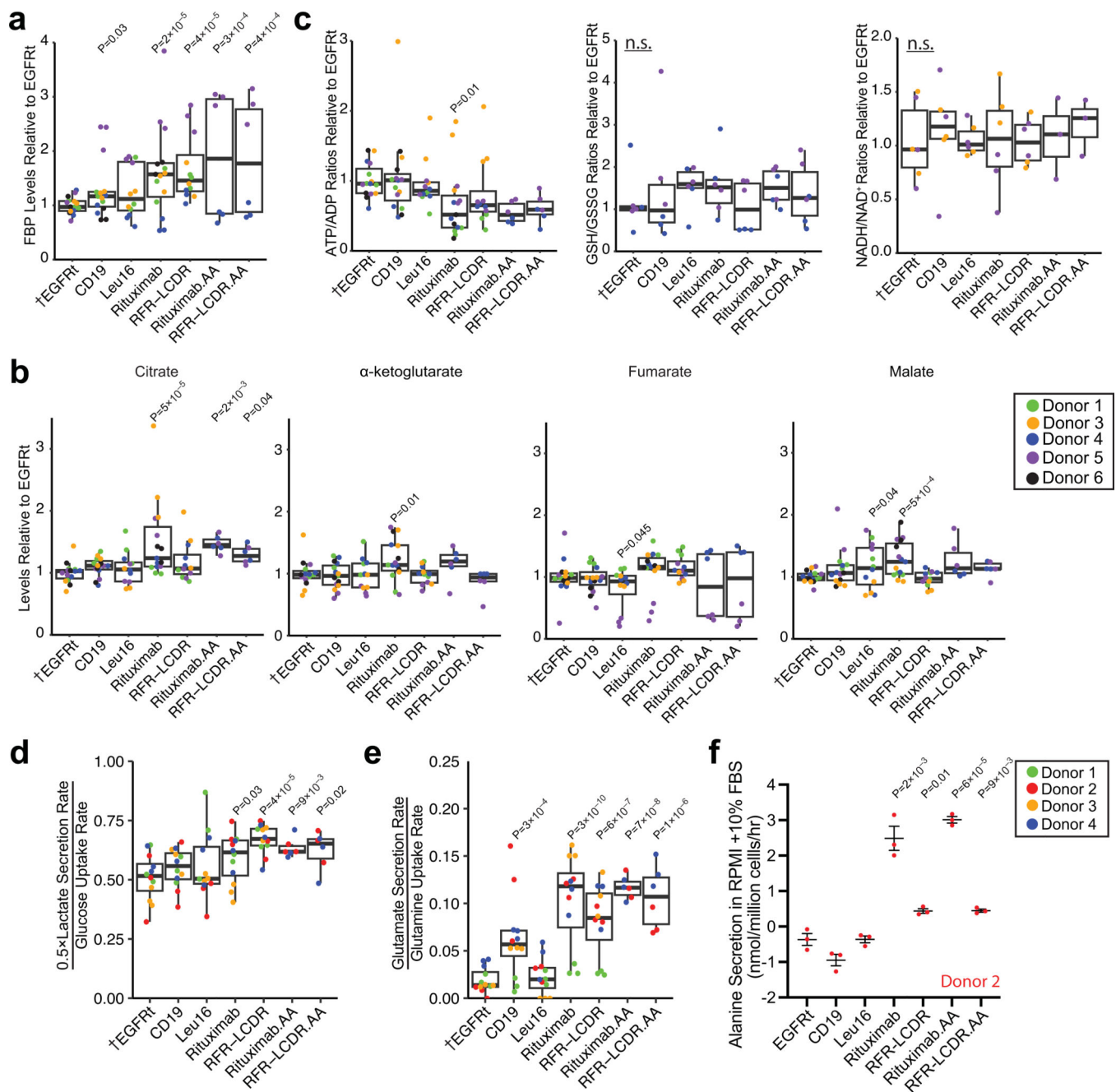
(a) Gating strategy for counting viable cells and quantifying their viability. Cell populations were gated for viable cells based on side-scatter area (SSC-A) vs. forward-scatter area (FSC-A) profiles. Viable cells were then gated for single cells based on FSC height (FSC-H) vs. FSC-A profiles. (b) CAR-T cells are viable up to 20 days post-retroviral transduction for Donor 6. Proliferation curves of CAR-T cells from days 17 to 20 post-transduction (left)

and viability of CAR-T cells on day 20 post-transduction (right) are shown. **(c)** Antibody staining of EGFRt (transduction marker), IgG4 extracellular spacer (Fc), and N-terminal HA tag was used to quantify transduction efficiencies and CAR surface expression by flow cytometry. The CD19 CAR lacks the CH2-CH3 domain of the IgG4 and cannot be detected via Fc staining. The CD19 CAR and Leu16 CAR lack the N-terminal HA tag. Each box shows the three quartiles (with the center line representing the median), and the whiskers extend to the minimum and maximum values that are within 1.5-fold of the interquartile range (n=2–6 biologically independent samples). **(d)** CAR-T cell phenotypes for Donor 2 (left) and Donor 5 (right). The subtypes of CAR-T cells in *in vitro* culture were determined by CD4, CD8, CD45RA, and CD62L staining in the absence of antigen stimulation. **(e)** Growth curves of CAR-T cells generated using primary human T cells from healthy donors showed that most CAR-T cells and EGFRt control T cells grew after a complete media change to RPMI-1640 media supplemented with dFBS, IL-2, and IL-15 on day 0. Cell counts between day 1 and the last time point for each donor were used to calculate proliferation rates. Panels (b) and (d) show the mean \pm s.e.m. with n=3 biological replicates. Statistical significance in panel (c) was determined using two-way analysis of variance (ANOVA) followed by Tukey's multiple comparison test to compare the pairwise differences in EGFRt, FC (anti-CD20 CAR-T cells only), and HA (rituximab, RFR-LCDR, rituximab.AA, and RFR-LCDR.AA) staining.



Extended Data Figure 2: The metabolome of EGFRt control T cells and CAR-T cells showed CAR-dependent metabolic profiles.

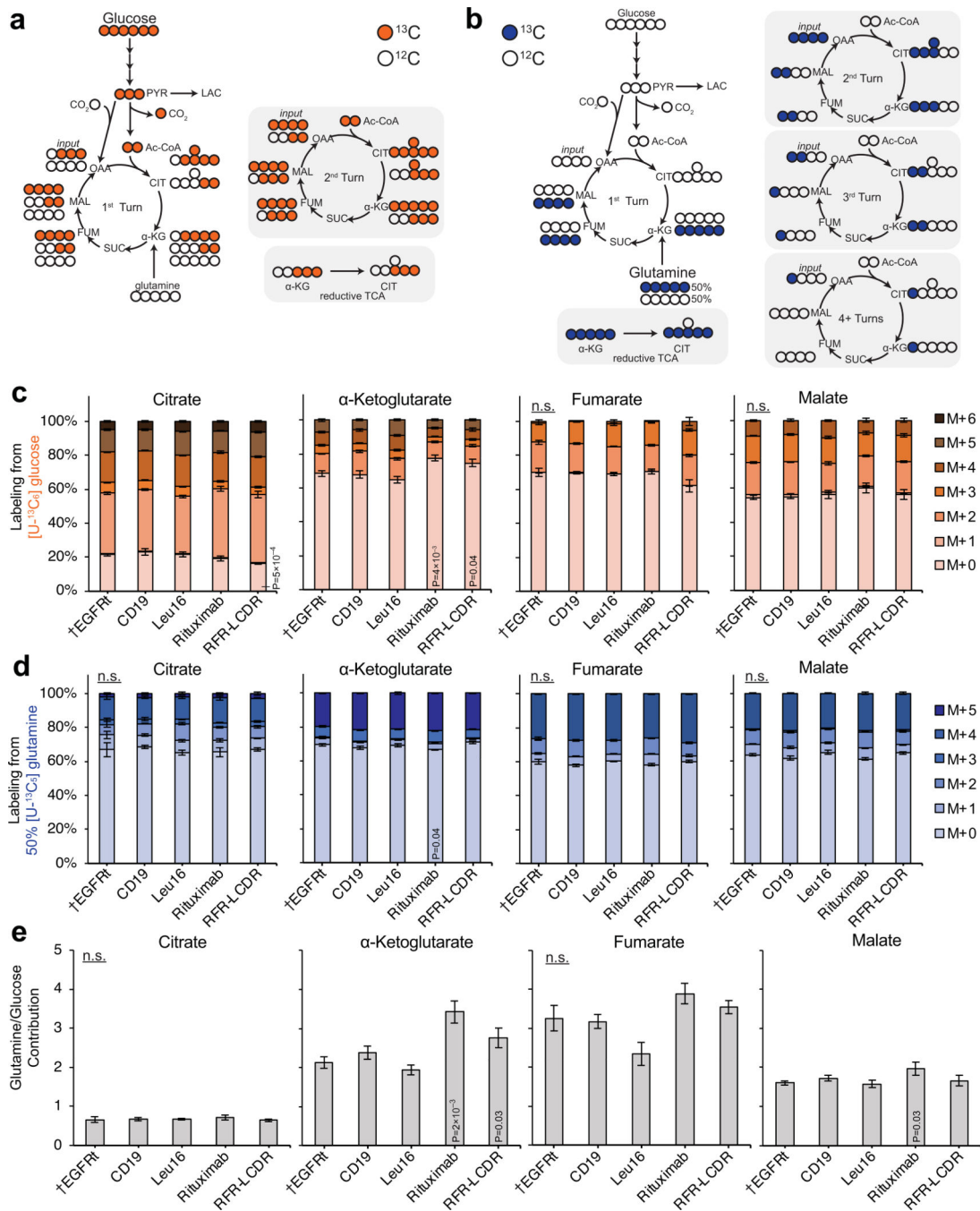
To account for batch effects, each metabolomics sample was normalized to its median ion count. Within each row, yellow and blue colors indicate higher and lower levels of a metabolite compared to the row mean of the respective donor CAR-T cells.



Extended Data Figure 3: Central carbon metabolites, co-factor ratios, and metabolite secretion.

(a) Fructose-1,6-bisphosphate (FBP) levels were higher in the four rituximab-based CAR-T cells than in EGFRt control T cells. (b) TCA cycle metabolites were higher in rituximab CAR-T cells than in EGFRt control T cells. (c) ATP/ADP was significantly lower in rituximab CAR-T cells, while glutathione/glutathione disulfide (GSH/GSSG) and NADH/NAD⁺ ratios showed no statistical difference. (d) Higher fractions of glucose-derived carbons were secreted as lactate by the four rituximab-based CAR-T cells than by EGFRt control T cells. The lactate-to-glucose carbon flux ratio represents fermentative glycolytic activity. (e) In anti-CD19 and rituximab-based CAR-T cells, higher fractions of glutamine

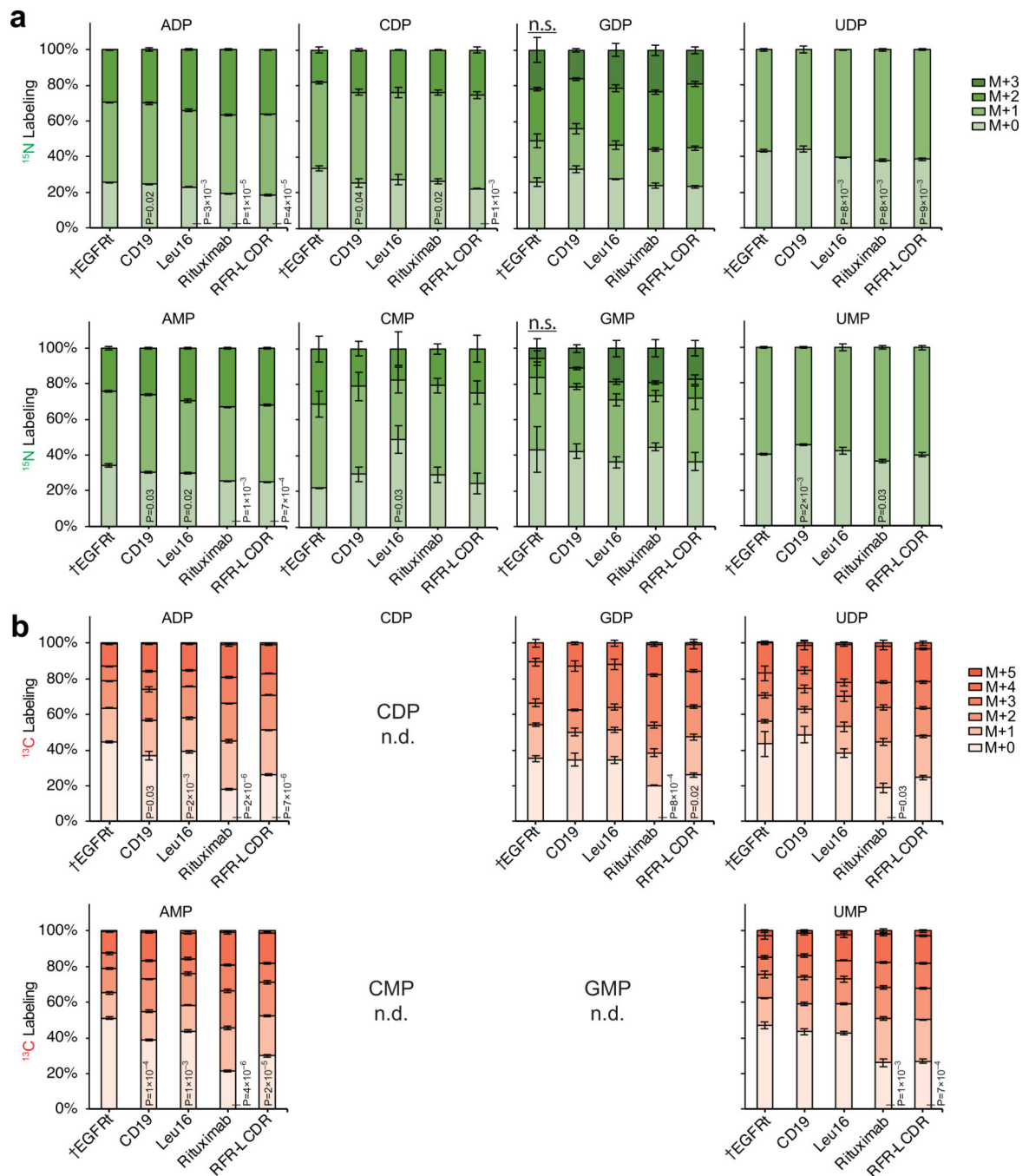
were diverted to glutamate secretion than in EGFRt control T cells. **(f)** Even in the presence of alanine in the media, rituximab-based CAR-T cells secreted alanine at substantial rates unlike EGFRt control T cells, anti-CD19 CAR-T cells, and Leu16 anti-CD20 CAR-T cells, which consumed alanine. Each box in panels (a)-(e) shows the three quartiles (with the center line representing the median), and the whiskers extend to the minimum and maximum values that are within 1.5-fold of the interquartile range (n=3–15 biological replicates from up to five donors). Metabolite levels in (a)-(c) are normalized to EGFRt control T cells, and the ratios are taken from the normalized metabolite levels. Statistical significance in panels (a)-(e) was determined by two-tailed *t* tests for a linear mixed-effects model (see Methods) in reference to EGFRt control T cells (†). Panel (f) shows the mean \pm s.e.m. with n=3 biological replicates. Statistical significance in panel (f) was determined by two-tailed *t* test in reference to EGFRt control T cells (†). n.s. indicates no statistical significance.



Extended Data Figure 4: The TCA cycle activity in CAR-T cells.

(a) $[\text{U-}^{13}\text{C}_6]\text{glucose}$ isotope tracing shows expected labeling patterns in the TCA cycle intermediates. (b) $[\text{U-}^{13}\text{C}_5]\text{glutamine}$ isotope tracing shows expected labeling patterns in the TCA cycle intermediates. (c) The contribution of glucose to α-ketoglutarate was lower in rituximab anti-CD20 CAR-T cells compared to that of EGFRt control T cells based on the significantly higher M+0 fraction in the former. EGFRt T cells and CAR-T cells from Donors 1 and 4 were labeled for 72 hours in media containing $[\text{U-}^{13}\text{C}_6]\text{glucose}$. Labeling fractions were corrected for natural isotope abundance and impurities. (d) Glutamine

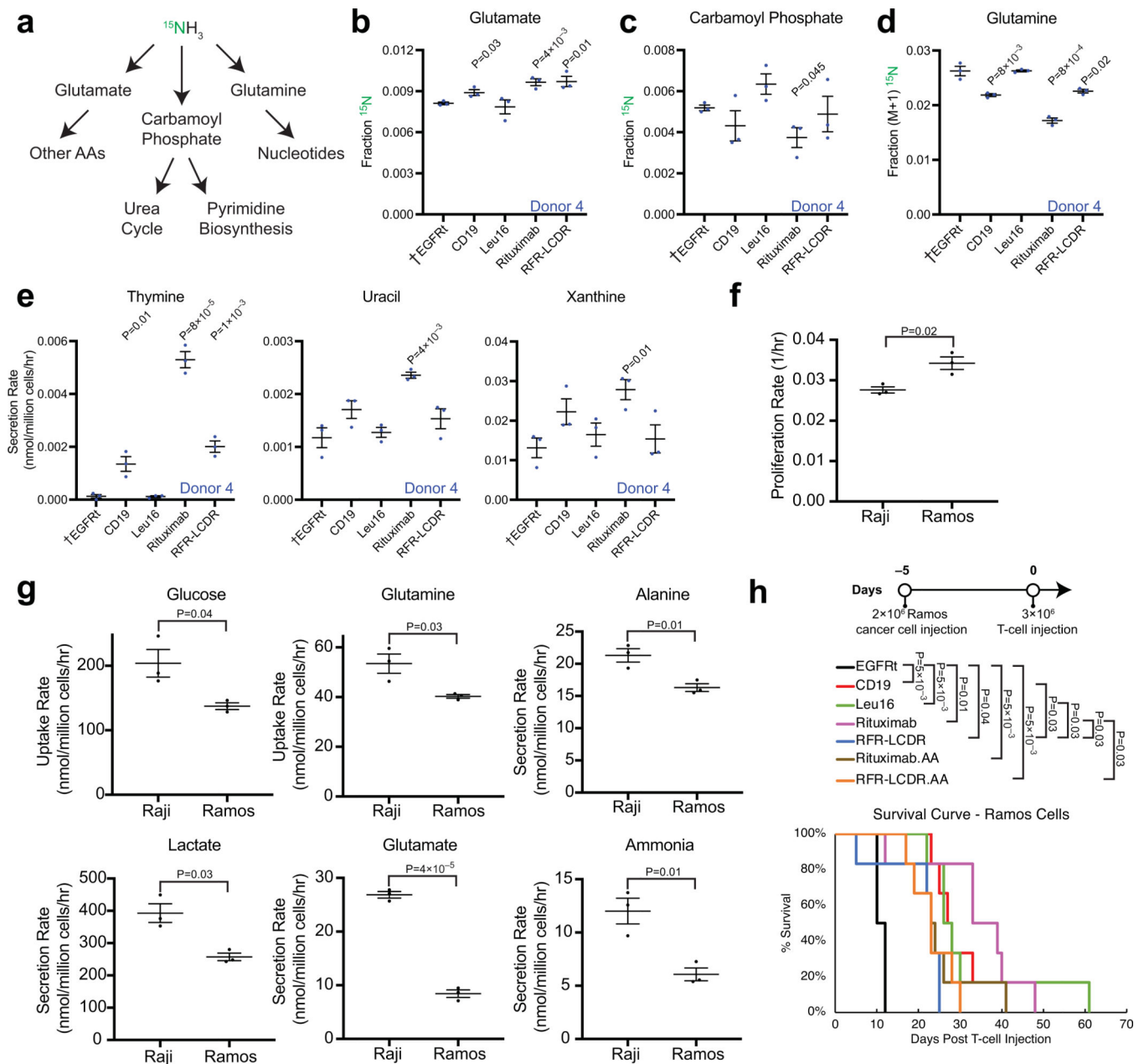
contribution to α -ketoglutarate was significantly higher in rituximab anti-CD20 CAR-T cells than in EGFRt control T cells. EGFRt T cells and CAR-T cells from Donor 3 were labeled for 48 hours in media containing 50% [U- $^{13}\text{C}_5$]glutamine. Labeling fractions were corrected for natural isotope abundance and impurities. (e) The relative contributions of glucose and glutamine on a carbon basis to the TCA cycle intermediates in the CAR-T cell panel indicated that citrate was derived mainly from glucose while the downstream TCA cycle metabolites were derived mainly from glutamine. Rituximab CAR-T cells displayed higher glutamine-to-glucose contribution ratios compared to EGFRt control T cells. The carbon contributions of glucose and glutamine were obtained by measuring the fractions of the total carbons ($^{12}\text{C}+^{13}\text{C}$) of individual metabolites that were ^{13}C and accounting for the enrichment fractions of the respective ^{13}C tracers (see Supplementary Note 5). Panel (c) shows the mean \pm s.e.m. with n=6 biological replicates. Panel (d) shows the mean \pm s.e.m. with n=3 biological replicates. Statistical significance in panels (c) and (d) was determined by two-tailed *t* tests in reference to EGFRt control T cells (†) for M+0 labeling. Panel (e) shows the mean \pm propagated error, and statistical significance was determined by bootstrapping (see Supplementary Note 5). n.s. indicates no statistical significance.



Extended Data Figure 5: Tracing nitrogen and carbon reveals nucleotide turnover.

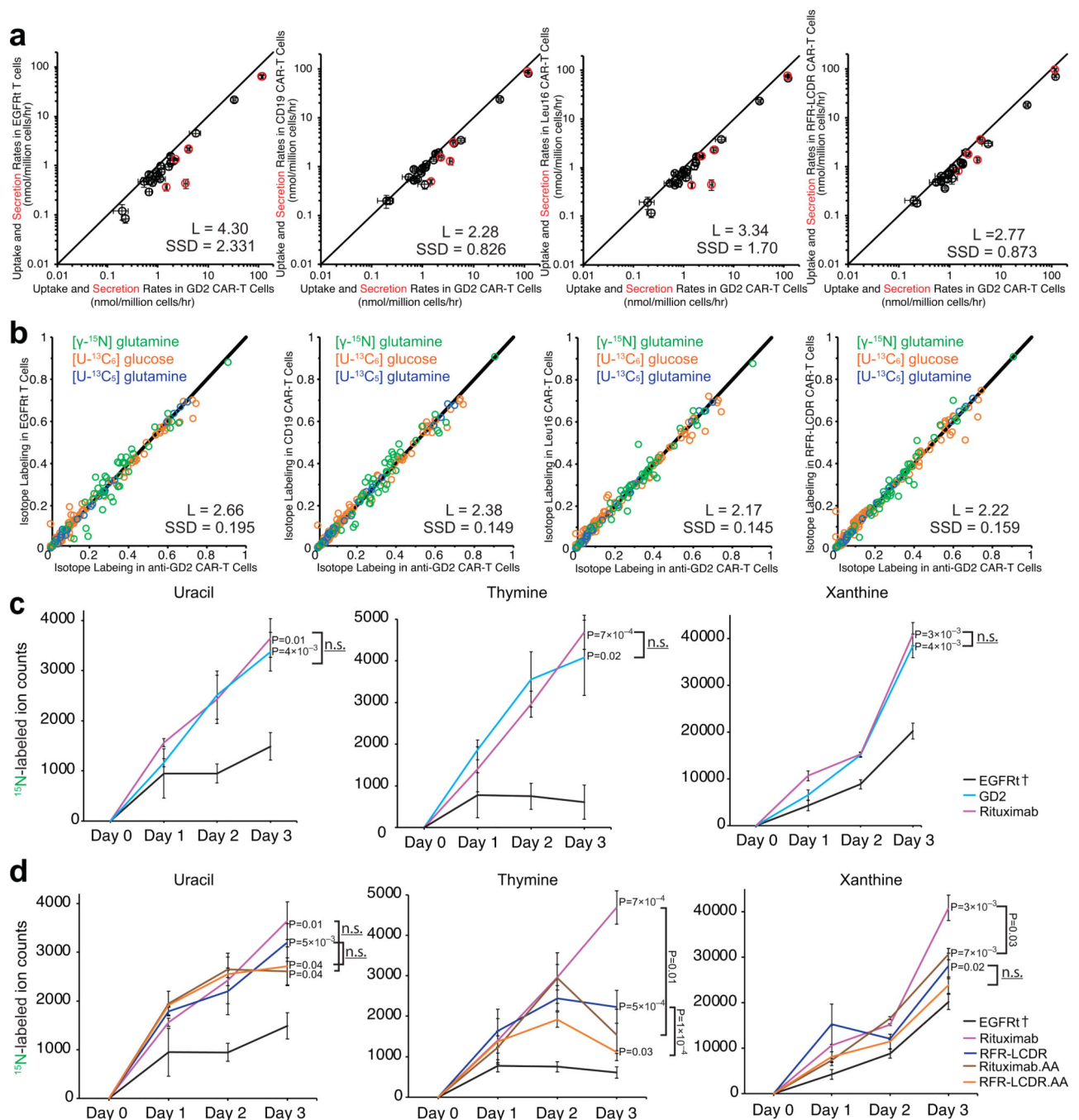
(a) EGFRt T cells and CAR-T cells from Donor 4 were cultured in media containing 50% [γ - ^{15}N]glutamine and 50% unlabeled glutamine for 72 hours. Adenosine diphosphate and monophosphate were labeled more in all CAR-T cells than in EGFRt control T cells. Uridine diphosphate in anti-CD20 CAR-T cells and many of the nucleotides in rituximab CAR-T cells were significantly more labeled than those of EGFRt control T cells. (b) EGFRt T cells and CAR-T cells from Donor 5 were cultured in media containing [1,2- $^{13}\text{C}_2$]glucose for 48 hours. Nucleotide diphosphates and monophosphates

were significantly more labeled in rituximab and RFR-LCDR CAR-T cells than in EGFRt control T cells. The greater labeling fractions in the same (48- and 72-hour) time periods indicated faster nucleotide turnover in rituximab and RFR-LCDR CAR-T cells. The signals of ^{13}C -labeled CDP, CMP, and GMP were too low to be reliable (n.d.). ^{13}C -labeling fractions were corrected for natural isotope abundance and impurities. Plots show the mean \pm s.e.m. with $n=3$ biological replicates. Statistical significance was determined by two-tailed t test in reference to EGFRt control T cells (\dagger) for M+0 labeling. n.s. indicates no statistical significance.



Extended Data Figure 6: Overflow metabolism and *in vivo* efficacy of CAR-T cells.

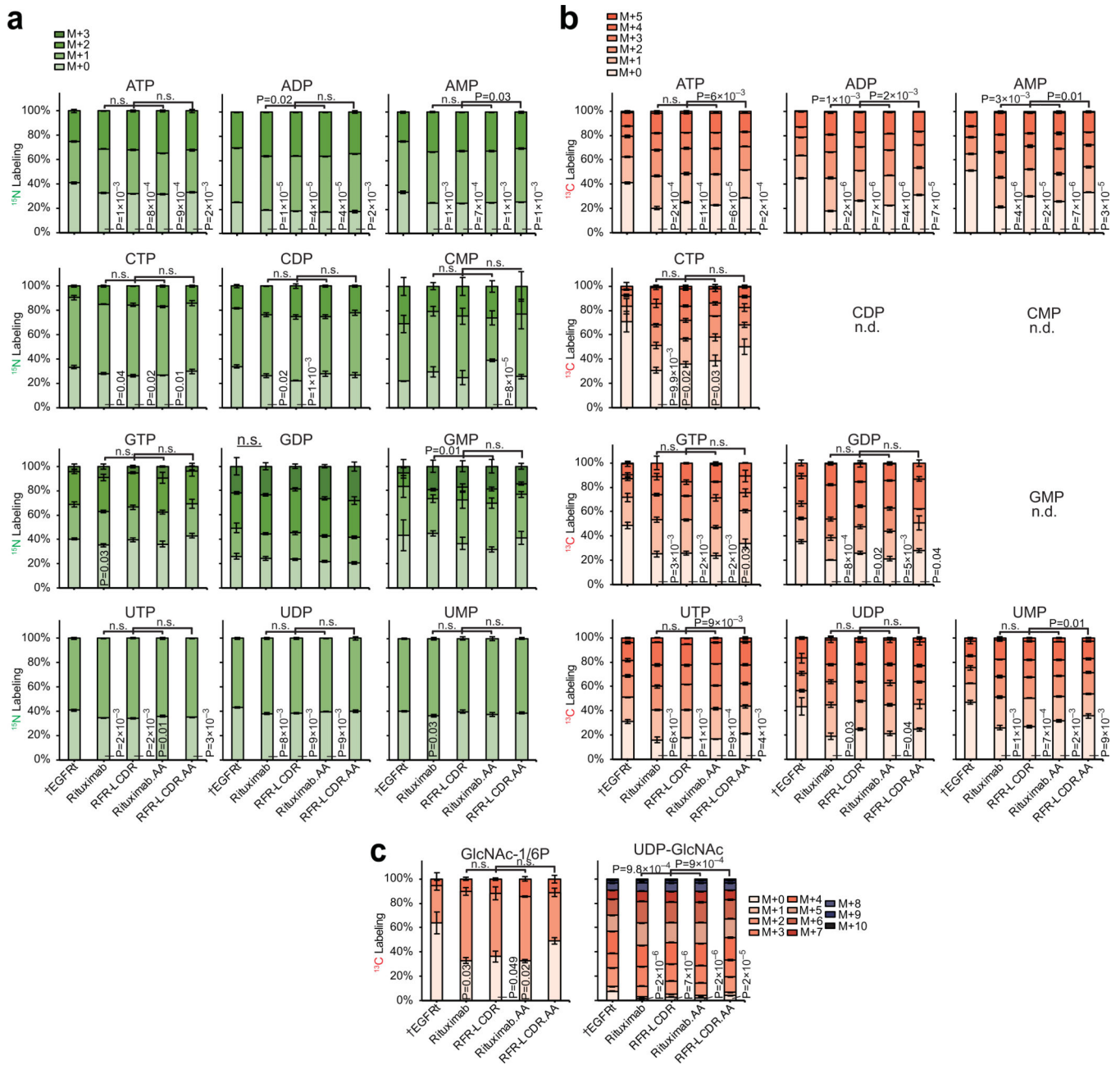
(a) Ammonia can be incorporated into metabolism via glutamate, glutamine, and carbamoyl phosphate. **(b-e)** EGFRt T cells and CAR-T cells from Donor 4 were cultured in media containing 800 μM $^{15}\text{NH}_4\text{Cl}$ for 72 hours. **(b)** Incorporation of ^{15}N from the labeled ammonia ($^{15}\text{NH}_3$) into glutamate was minimal in all T cells but significantly higher for anti-CD19 and rituximab-based anti-CD20 CAR-T cells compared with EGFRt control T cells. **(c)** Incorporation of ^{15}N from $^{15}\text{NH}_3$ into carbamoyl phosphate was minimal in all T cells but significantly lower for rituximab CAR-T cells compared with EGFRt T cells. **(d)** Incorporation of ^{15}N from $^{15}\text{NH}_3$ into glutamine was significantly lower for anti-CD19 and rituximab-based anti-CD20 CAR-T cells compared with EGFRt control T cells. **(e)** EGFRt T cells and CAR-T cells secreted thymine, uracil, and xanthine. **(f-g)** Raji and Ramos lymphoma cells were cultured for 48 hours. **(f)** Proliferation rates were determined based on the changes in cell numbers between day 1 and day 2. **(g)** Nutrient uptake and byproduct secretion rates were compared between Raji and Ramos cells. **(h)** Kaplan-Meier survival curve against Ramos cancer cells. NOD/SCID/IL-2R γ^{null} (NSG) mice (n=6 animals) were injected intravenously with Ramos cells and subsequently treated with control (EGFRt), anti-CD19, or anti-CD20 CAR T cells. In panels (b)-(e), plots show the mean \pm s.e.m. with n=3 biological replicates, and statistical significance was determined by two-tailed *t* tests in reference to EGFRt control T cells (\dagger). Panels (f)-(g) show the mean \pm s.e.m. with n=3 biological replicates, and statistical significance was determined by two-tailed *t* tests. Statistical significance in panel (h) was determined by multiple log-rank (Mantel-Cox) tests with adjustment using the Benjamini-Hochberg FDR controlling procedure.



Extended Data Figure 7: Comparison of metabolic fluxes across CAR-T cell variants.

(a) Anti-GD2 CAR-T cells were more similar to rituximab CAR-T cells than any other CAR-T cell variants in terms of nutrient uptake rates (black) and byproduct secretion rates (red) (*cf.* Fig. 6b). SSD is the sum of squared differences, and L is the total distance between individual points and the line of unity. Plot shows the mean \pm s.e.m. with $n=12$ biological replicates for EGFRt control T cells and anti-CD20 CAR-T cells and $n=6$ biological replicates for anti-GD2 CAR-T cells. (b) Metabolite labeling patterns in CAR-T cells, which were fed 50% [γ - ^{15}N]glutamine, [U - $^{13}\text{C}_6$]glucose, and [U - $^{13}\text{C}_5$]glutamine, showed

the greatest similarity between 14g2a-based anti-GD2 CAR-T cells and rituximab CAR-T cells (*cf.* Fig. 6c). **(c-d)** EGFRt T cells and CAR-T cells from Donor 4 were cultured in media containing 50% [γ - ^{15}N]glutamine for 72 hours. ^{15}N -labeled pyrimidine and purine nucleobases were measured from media samples collected each day. Ion counts for xanthine represent the sum of M+1 and M+2 ^{15}N -labeled ions. **(c)** Rituximab anti-CD20 and 14g2a anti-GD2 CAR-T cells displayed similarly high accumulation of purine and pyrimidine nucleobases. **(d)** The four rituximab-based CAR-T cells had faster nucleotide degradation than EGFRt control T cells. Alanine insertions in the non-signaling intracellular domains of CARs resulted in significant differences in thymine secretion. Panels (c) and (d) show the mean \pm s.e.m. with $n=3$ biological replicates, and statistical significance was determined by two-tailed t tests in reference to the day-3 media sample from EGFRt control T cells (\dagger). Further statistical tests were conducted between rituximab and anti-GD2 CAR-T cells, rituximab and rituximab.AA CAR-T cells, and RFR-LCDR and RFR-LCDR.AA CAR-T cells for day-3 nucleobase measurements. n.s. indicates no statistical significance.



Extended Data Figure 8: Tracing nitrogen and carbon in nucleotide and hexosamine biosynthesis in CAR-T cells with two-alanine insertions.

(a) EGFRt T cells and CAR-T cells from Donor 4 were cultured in media containing 50% [γ - ^{15}N]glutamine for 72 hours. Many nucleotides were labeled more in rituximab-based CAR-T cells than in EGFRt control T cells. Alanine insertions resulted in minimal differences. (b-c) EGFRt T cells and CAR-T cells from Donor 5 were cultured in media containing [$1,2$ - $^{13}\text{C}_2$]glucose for 48 hours. (b) Many nucleotides were labeled more in rituximab-based CAR-T cells than in the EGFRt control T cells. Alanine insertions resulted in minimal differences. The signals of ^{13}C -labeled CDP, CMP, and GMP were too low to be reliable (n.d.). (c) N-acetylglucosamine-1/6-phosphate (GlcNAc-1/6P) and UDP-N-

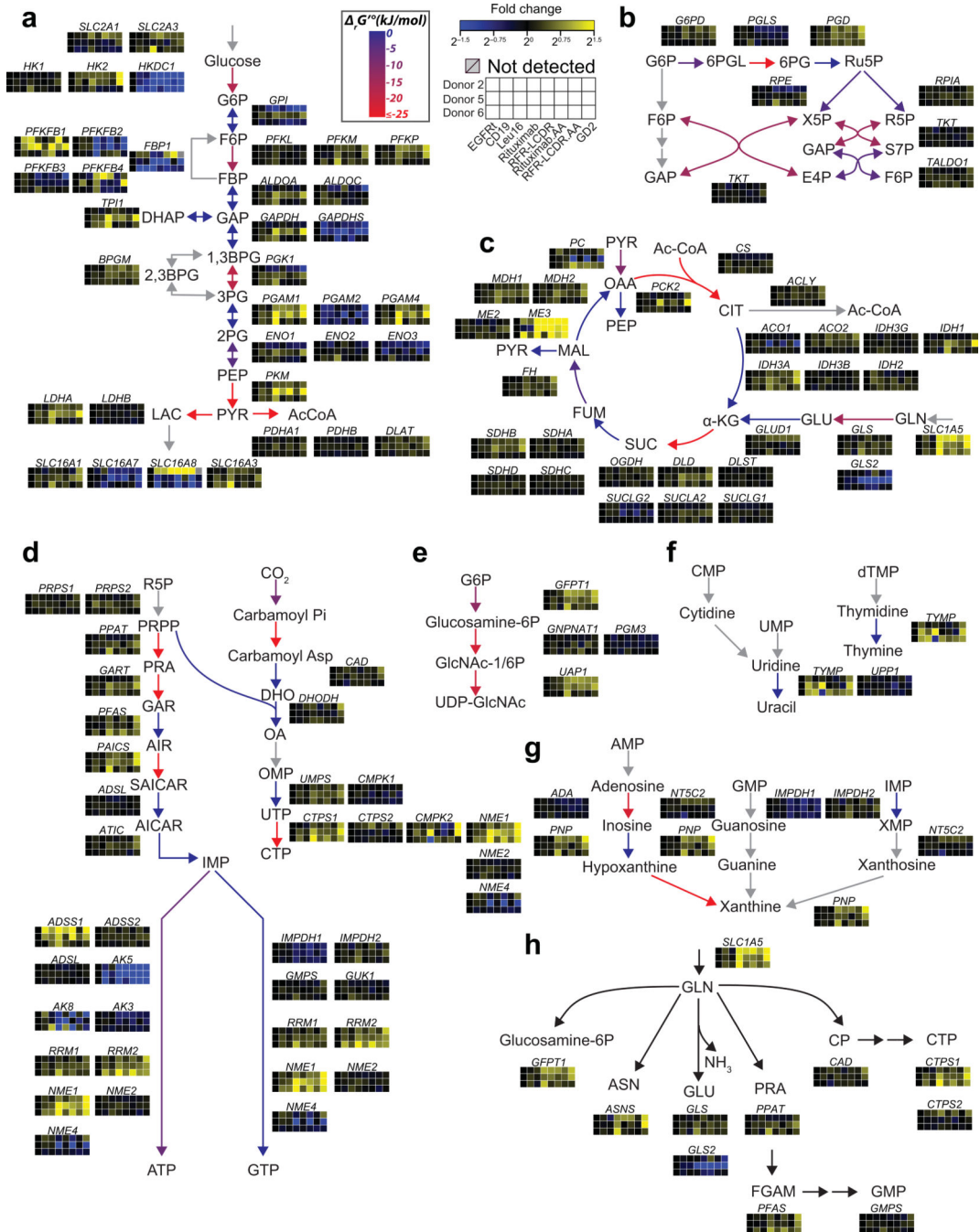
acetylglucosamine (UDP-GlcNAc) were labeled more in rituximab-based CAR-T cells than in EGFRt control T cells. Rituximab.AA and RFR-LCDR.AA CAR-T cells with alanine insertions increased M+0 fractions of UDP-GlcNAc compared with rituximab and RFR-LCDR CAR-T cells, respectively. ^{13}C -labeling fractions were corrected for natural isotope abundance and impurities. Plots show the mean \pm s.e.m. with n=3 biological replicates. Statistical significance of the observed M+0 labeling fractions was determined by two-tailed *t* test in reference to EGFRt control T cells (\dagger), between rituximab and rituximab.AA CAR-T cells, and between RFR-LCDR and RFR-LCDR.AA CAR-T cells. n.s. indicates no statistical significance.

Author Manuscript

Author Manuscript

Author Manuscript

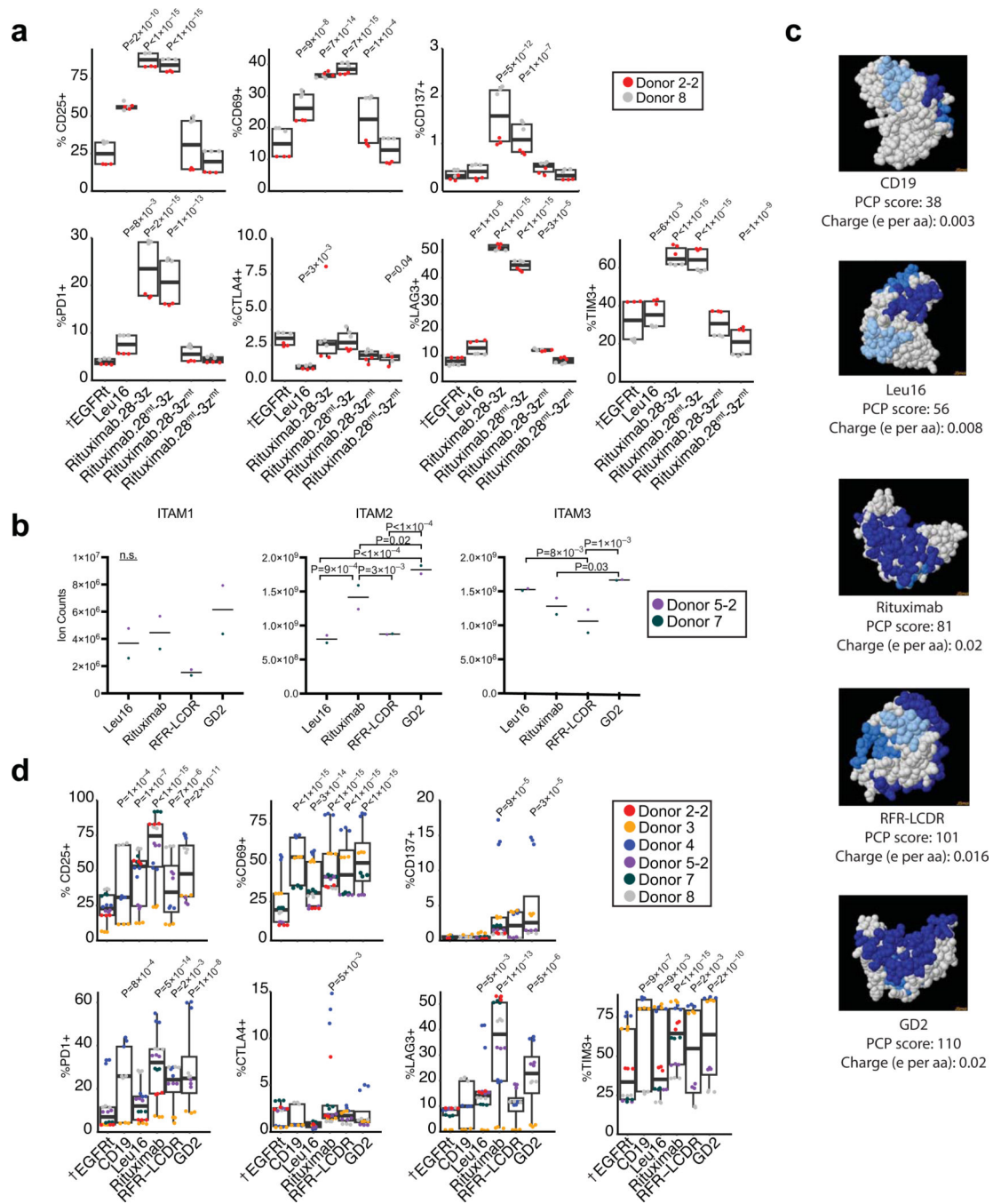
Author Manuscript



Extended Data Figure 9: CAR-T cells were cultured in the absence of antigen stimulation for RNA-seq.

Across three donors, genes associated with (a) glycolysis, (b) the pentose phosphate pathway, (c) the TCA cycle, (d) nucleotide biosynthesis, (e) hexosamine biosynthesis, (f) pyrimidine degradation, (g) purine degradation, and (h) glutamine metabolism are shown. Each row indicates a donor (Donor 2, 5, or 6). Within each row, yellow and blue colors indicate higher and lower levels of the transcript compared with EGFRt control T cells. Arrow colors represent the standard Gibbs free energy of reaction ΔG° , which

approximates the extent of metabolic flux control based on how close to or far away from equilibrium the reaction is.



Extended Data Figure 10: Electrostatic property and phosphorylation of CARs may affect T-cell activation and exhaustion.

(a) Activation- (top row) and exhaustion-marker (bottom row) expression on mutant rituximab CAR-T cells were compared to EGFRt, Leu16 CAR-, and rituximab CAR-T cells (n=6 biological replicates from two donors). (b) Phosphorylation of the signaling domains of CARs including the three ITAM regions of CD3 ζ was measured (n=2 biologically

independent samples). Even with good peptide sequence coverage, CD28 phosphopeptide was below the limit of detection. (c) Top three largest positively charged patches (PCPs) containing continuous positive charged residues are shown in each scFv. Dark blue, largest PCP; medium blue, second largest PCP; light blue, third largest PCP. PCP score (sum of the number of residues in the three largest PCPs) and charge per amino acid are displayed under each construct. (d) Activation- (top row) and exhaustion-marker (bottom row) expression on CAR-T cells were evaluated on day 2 or 3 without antigen stimulation (n=12–18 biological replicates from up to six donors). Donors 2–2 and 5–2 represent second batches of transduced cells from Donors 2 and 5, respectively. Each box in panels (a) and (d) shows the three quartiles (with the center line representing the median), and the whiskers extend to the minimum and maximum values that are within 1.5-fold of the interquartile range. Statistical significance for activation and exhaustion markers in panels (a) and (d) was determined by two-tailed *t* tests for a linear mixed-effects model (see Methods) in reference to EGFRt control T cells (†). Statistical significance in panel (b) was determined using two-way analysis of variance (ANOVA) followed by Tukey's multiple comparison test to compare the pairwise differences in ITAM1, ITAM2, and ITAM3 phosphorylation.

Supplementary Material

Refer to Web version on PubMed Central for supplementary material.

Acknowledgements

The authors would like to thank the members of the Park lab, the UCLA Molecular Instrumentation Center, the UCLA Metabolomics Center, and the UCLA Proteome Research Center as well as Drs. M. Nofal, L. B. Tanner, Y. Song, A. M. Wu, M. C. Jensen, S. Rosenberg, and S. Feldman. This work was supported by the National Institute of General Medical Sciences of the National Institutes of Health under Award Number R35GM143127 (J.O.P.), the National Institutes of Health Instrumentation Grant Number 1S10OD016387-01, the National Institutes of Health Biotechnology Training Grant under Award Number T32GM067555 (A.L.), the Alliance for Cancer Gene Therapy Young Investigator Award (Y.Y.C.), the Cancer Research Institute Lloyd J. Old STAR Award (Y.Y.C.), and the UCLA Jonsson Comprehensive Cancer Center Intramural Award (Y.Y.C. and J.O.P.).

Competing Interests

X.C. and Y.Y.C. are inventors of a patent whose value may be affected by the publication of this work. Y.Y.C. holds several patent applications in the area of CAR-T cell therapy. Y.Y.C. is a founder of, holds equity in, and receives consulting fees from ImmPACT Bio. Y.Y.C. is a member of the scientific advisory board of and holds equity in Catamaran Bio, Notch Therapeutics, Pluto Immunotherapeutics, Prime Medicine, Sonoma Biotherapeutics, and Waypoint Bio.

Data availability

Source data for Figures 1–6 are provided in Supplementary Tables 1–23 and the GitHub public repository: <https://github.com/aliyalakhani/CAR-T-Cell-Metabolism>

Raw MS data and search results for phosphopeptides are placed in the MassIVE public repository: <https://massive.ucsd.edu/ProteoSAFe/dataset.jsp?task=ab1708b9ae434f6082da533fcf27870a> (Project ID number: MSV000093637)

Raw RNA-seq data for transcriptomics are placed in the National Center for Biotechnology Information Sequence Read Archive (NCBI SRA): <https://www.ncbi.nlm.nih.gov/bioproject/PRJNA1085526> (Accession number: PRJNA1085526)

The sequence and structure for the 14g2a mAb is provided through the Protein Data Bank: <https://doi.org/10.2210/pdb4TUJ/pdb> (PDB 4TUJ)

Source data are provided for this paper.

References

1. Ho P. & Chen YY Synthetic Biology in Immunotherapy and Stem Cell Therapy Engineering. in *Synthetic Biology* 349–372 (Wiley-VCH Verlag GmbH & Co. KGaA, 2018). doi:10.1002/9783527688104.ch17.
2. Brudno JN et al. T Cells Genetically Modified to Express an Anti-B-Cell Maturation Antigen Chimeric Antigen Receptor Cause Remissions of Poor-Prognosis Relapsed Multiple Myeloma. *J. Clin. Oncol* 36, 2267–2280 (2018). [PubMed: 29812997]
3. Cohen AD et al. Safety and Efficacy of B-Cell Maturation Antigen (BCMA)-Specific Chimeric Antigen Receptor T Cells (CART-BCMA) with Cyclophosphamide Conditioning for Refractory Multiple Myeloma (MM). *Blood* 130, 505–505 (2017).
4. Majzner RG & Mackall CL Clinical lessons learned from the first leg of the CAR T cell journey. *Nat. Med* vol. 25 1341–1355 (Nature Publishing Group, 2019). [PubMed: 31501612]
5. Rafiq S, Hackett CS & Brentjens RJ Engineering strategies to overcome the current roadblocks in CAR T cell therapy. *Nat. Rev. Clin. Oncol* 2019 173 17, 147–167 (2019).
6. Geiger R. et al. L-Arginine Modulates T Cell Metabolism and Enhances Survival and Anti-tumor Activity. *Cell* 167, 829–842.e13 (2016). [PubMed: 27745970]
7. Can E. et al. Noninvasive rapid detection of metabolic adaptation in activated human T lymphocytes by hyperpolarized ¹³C magnetic resonance. *Sci. Reports* 2020 101 10, 1–8 (2020).
8. Levine LS et al. Single-cell analysis by mass cytometry reveals metabolic states of early-activated CD8+ T cells during the primary immune response. *Immunity* 54, 829–844.e5 (2021). [PubMed: 33705706]
9. Wang R. et al. The Transcription Factor Myc Controls Metabolic Reprogramming upon T Lymphocyte Activation. *Immunity* (2011) doi:10.1016/j.immuni.2011.09.021.
10. Blagih J. et al. The Energy Sensor AMPK Regulates T Cell Metabolic Adaptation and Effector Responses InVivo. *Immunity* 42, 41–54 (2015). [PubMed: 25607458]
11. Ron-Harel N. et al. Mitochondrial Biogenesis and Proteome Remodeling Promote One-Carbon Metabolism for T Cell Activation. *Cell Metab.* 24, 104–117 (2016). [PubMed: 27411012]
12. Klein Geltink RI et al. Metabolic conditioning of CD8+ effector T cells for adoptive cell therapy. *Nat. Metab* 2, (2020).
13. Bantug GR, Galluzzi L, Kroemer G. & Hess C. The spectrum of T cell metabolism in health and disease. *Nature Reviews Immunology* vol. 18 19–34 (2018).
14. Vardhana SA et al. Impaired mitochondrial oxidative phosphorylation limits the self-renewal of T cells exposed to persistent antigen. *Nat. Immunol* 21, (2020).
15. Liu X. et al. Affinity-Tuned ErbB2 or EGFR Chimeric Antigen Receptor T Cells Exhibit an Increased Therapeutic Index against Tumors in Mice. *Cancer Res.* 75, 3596–3607 (2015). [PubMed: 26330166]
16. Lu J. & Jiang G. The journey of CAR-T therapy in hematological malignancies. *Mol. Cancer* 2022 211 21, 1–15 (2022).
17. Majzner RG & Mackall CL Tumor Antigen Escape from CAR T-cell Therapy. *Cancer Discov.* 8, 1219–26 (2018). [PubMed: 30135176]
18. Horna P, Nowakowski G, Endell J. & Boxhammer R. Comparative Assessment of Surface CD19 and CD20 Expression on B-Cell Lymphomas from Clinical Biopsies: Implications for Targeted Therapies. *Blood* 134, (2019).
19. Till BG et al. CD20-specific adoptive immunotherapy for lymphoma using a chimeric antigen receptor with both CD28 and 4–1BB domains: Pilot clinical trial results. *Blood* 119, 3940–3950 (2012). [PubMed: 22308288]

20. Larson SM et al. CD19/CD20 Bispecific Chimeric Antigen Receptor (CAR) in Naive/Memory T Cells for the Treatment of Relapsed or Refractory Non-Hodgkin Lymphoma. *Cancer Discov.* 13, 580–597 (2023). [PubMed: 36416874]
21. Salles G. et al. Rituximab in B-Cell Hematologic Malignancies: A Review of 20 Years of Clinical Experience. *Adv. Ther.* 2017 34(10) 34, 2232–2273 (2017).
22. Chen X. et al. Rational Protein Design Yields a CD20 CAR with Superior Antitumor Efficacy Compared with CD19 CAR. *Cancer Immunol. Res* OF1–OF14 (2022) doi:10.1158/2326-6066.CIR-22-0504.
23. Long AH et al. 4–1BB costimulation ameliorates T cell exhaustion induced by tonic signaling of chimeric antigen receptors. *Nat. Med* 21, 581 (2015). [PubMed: 25939063]
24. Mössner E. et al. Increasing the efficacy of CD20 antibody therapy through the engineering of a new type II anti-CD20 antibody with enhanced direct and immune effector cell - mediated B-cell cytotoxicity. *Blood* 115, 4393–4402 (2010). [PubMed: 20194898]
25. Uchiyama S. et al. Development of novel humanized anti-CD20 antibodies based on affinity constant and epitope. *Cancer Sci.* 101, 201–209 (2010). [PubMed: 19930155]
26. Tanner LB et al. Four Key Steps Control Glycolytic Flux in Mammalian Cells. *Cell Syst.* 7, (2018).
27. Hosios AM et al. Amino Acids Rather than Glucose Account for the Majority of Cell Mass in Proliferating Mammalian Cells. *Dev. Cell* 36, 540–549 (2016). [PubMed: 26954548]
28. Kelly B. & Pearce EL Amino Assets: How Amino Acids Support Immunity. *Cell Metab.* 32, 154–175 (2020). [PubMed: 32649859]
29. Hope HC et al. Coordination of asparagine uptake and asparagine synthetase expression modulates CD8+ T cell activation. *JCI Insight* 6, (2021).
30. Ron-Harel N. et al. T Cell Activation Depends on Extracellular Alanine. *Cell Rep.* 28, (2019).
31. Kaymak I. et al. Carbon source availability drives nutrient utilization in CD8+ T cells. *Cell Metab.* 34, 1298–1311.e6 (2022). [PubMed: 35981545]
32. Scherer S. et al. Pyrimidine de novo synthesis inhibition selectively blocks effector but not memory T cell development. *Nat. Immunol* | 24, 26 (2023).
33. Wellen KE & Thompson CB Cellular metabolic stress: Considering how cells respond to nutrient excess. *Mol. Cell* 40, 323 (2010). [PubMed: 20965425]
34. Bond MR & Hanover JA A little sugar goes a long way: The cell biology of O-GlcNAc. *J. Cell Biol* 208, 869–880 (2015). [PubMed: 25825515]
35. Butkinaree C, Park K. & Hart GW O-linked β -N-acetylglucosamine (O-GlcNAc): Extensive crosstalk with phosphorylation to regulate signaling and transcription in response to nutrients and stress. *Biochim. Biophys. Acta - Gen. Subj* 1800, 96–106 (2010).
36. Swamy M. et al. Glucose and glutamine fuel protein O-GlcNAcylation to control T cell self-renewal and malignancy. *Nat. Immunol* 17, 712–720 (2016). [PubMed: 27111141]
37. Bell HN et al. Microenvironmental ammonia enhances T cell exhaustion in colorectal cancer. *Cell Metab.* 35, 134–149.e6 (2023). [PubMed: 36528023]
38. Spinelli JB et al. Metabolic recycling of ammonia via glutamate dehydrogenase supports breast cancer biomass. *Science* (80-.) 358, 941–946 (2017).
39. Tessem MB et al. Evaluation of lactate and alanine as metabolic biomarkers of prostate cancer using 1H HR-MAS spectroscopy of biopsy tissues. *Magn. Reson. Med* 60, 510–516 (2008). [PubMed: 18727052]
40. Quinn WJ et al. Lactate Limits T Cell Proliferation via the NAD(H) Redox State. *Cell Rep.* 33, 108500 (2020).
41. Angelin A. et al. Foxp3 Reprograms T Cell Metabolism to Function in Low-Glucose, High-Lactate Environments. *Cell Metab.* 25, 1282–1293.e7 (2017). [PubMed: 28416194]
42. Park JO et al. Near-equilibrium glycolysis supports metabolic homeostasis and energy yield. *Nat. Chem. Biol* 15, (2019).
43. Fell DA, Lee SY, Nielsen J. & Stephanopoulos G. Metabolic Control Analysis. *Metab. Eng. Concepts Appl* Vol. 13a 13b 13, 171–211 (2021).
44. Lindner SE, Johnson SM, Brown CE & Wang LD Chimeric antigen receptor signaling: Functional consequences and design implications. *Sci. Adv* 6, (2020).

45. Moeller M. et al. A functional role for CD28 costimulation in tumor recognition by single-chain receptor-modified T cells. *Cancer Gene Ther.* 2004 115 11, 371–379 (2004).
46. Chang ZL et al. Rewiring T-cell responses to soluble factors with chimeric antigen receptors. *Nat. Chem. Biol* 14, (2018).
47. Zhao Y. et al. A herceptin-based chimeric antigen receptor with modified signaling domains leads to enhanced survival of transduced T lymphocytes and antitumor activity. *J. Immunol* 183, 5563–5574 (2009). [PubMed: 19843940]
48. Chen J. et al. Tuning charge density of chimeric antigen receptor optimizes tonic signaling and CAR-T cell fitness. *Cell Res.* 2023 335 33, 341–354 (2023).
49. Zhang X, Zhu L, Zhang H, Chen S. & Xiao Y. CAR-T Cell Therapy in Hematological Malignancies: Current Opportunities and Challenges. *Frontiers in Immunology* vol. 13 (2022).
50. Subklewe M, Von Bergwelt-Baildon M. & Humpe A. Chimeric Antigen Receptor T Cells: A Race to Revolutionize Cancer Therapy. *Transfusion Medicine and Hemotherapy* vol. 46 (2019).
51. Kawalekar OU et al. Distinct Signaling of Coreceptors Regulates Specific Metabolism Pathways and Impacts Memory Development in CAR T Cells. *Immunity* 44, 380–390 (2016). [PubMed: 26885860]
52. Hirabayashi K. et al. Dual Targeting CAR-T Cells with Optimal Costimulation and Metabolic Fitness enhance Antitumor Activity and Prevent Escape in Solid Tumors. *Nat. cancer* 2, 904–918 (2021). [PubMed: 34746799]
53. Hudecek M. et al. The non-signaling extracellular spacer domain of chimeric antigen receptors is decisive for in vivo antitumor activity. 3, (2015).
54. Reaves ML, Young BD, Hosios AM, Xu YF & Rabinowitz JD Pyrimidine homeostasis is accomplished by directed overflow metabolism. *Nature* 500, (2013).
55. Kurmi K. & Haigis MC Nitrogen Metabolism in Cancer and Immunity. *Trends Cell Biol.* 30, 408 (2020). [PubMed: 32302552]
56. Chae WJ et al. Qualitatively differential regulation of T cell activation and apoptosis by T cell receptor ζ chain ITAMs and their tyrosine residues. *Int. Immunol* 16, 1225–1236 (2004). [PubMed: 15302845]
57. Nicholson IC et al. Construction and characterisation of a functional CD19 specific single chain Fv fragment for immunotherapy of B lineage leukaemia and lymphoma. *Mol. Immunol* 34, (1997).
58. Zettlitz KA et al. ImmunoPET of Malignant and Normal B Cells with 89Zr- and 124I-Labeled Obinutuzumab Antibody Fragments Reveals Differential CD20 Internalization In Vivo. *Clin. Cancer Res* 23, 7242–7252 (2017). [PubMed: 28928164]
59. Jensen M, Tan G, Forman S, Wu AM & Raubitschek A. CD20 is a molecular target for scFvFc: ζ receptor redirected T cells: Implications for cellular immunotherapy of CD10+ malignancy. *Biol. Blood Marrow Transplant* 4, 75–83 (1998). [PubMed: 9763110]
60. Madeira F. et al. Search and sequence analysis tools services from EMBL-EBI in 2022. *Nucleic Acids Res.* 50, (2022).
61. Mitchell DM, Ravkov EV & Williams MA Distinct roles for IL-2 and IL-15 in the differentiation and survival of CD8+ effector and memory T cells. *J. Immunol* 184, 6719 (2010). [PubMed: 20483725]
62. Van Acker HH et al. Interleukin-15 enhances the proliferation, stimulatory phenotype, and antitumor effector functions of human gamma delta T cells. *J. Hematol. Oncol* 9, 1–13 (2016). [PubMed: 26733151]
63. Park JO et al. Metabolite concentrations, fluxes and free energies imply efficient enzyme usage. *Nat. Chem. Biol* 12, 482–489 (2016). [PubMed: 27159581]
64. Wang L. et al. Peak Annotation and Verification Engine for Untargeted LC-MS Metabolomics. *Anal. Chem* 91, (2019).
65. Seitzer P, Bennett B. & Melamud E. MAVEN2: An Updated Open-Source Mass Spectrometry Exploration Platform. *Metabolites* 12, (2022).
66. Antoniewicz MR, Kelleher JK & Stephanopoulos G. Elementary metabolite units (EMU): A novel framework for modeling isotopic distributions. *Metab. Eng* 9, (2007).

67. Antoniewicz MR, Kelleher JK & Stephanopoulos G. Determination of confidence intervals of metabolic fluxes estimated from stable isotope measurements. *Metab. Eng* 8, 324–337 (2006). [PubMed: 16631402]
68. Andrews S. FastQC: A Quality Control Tool for High Throughput Sequence Data [Online]. (2010).
69. Martin M. Cutadapt removes adapter sequences from high-throughput sequencing reads. *EMBnet.journal* 17, 10–12 (2011).
70. Kim D. et al. TopHat2: Accurate alignment of transcriptomes in the presence of insertions, deletions and gene fusions. *Genome Biol.* 14, 1–13 (2013).
71. Liao Y, Smyth GK & Shi W. featureCounts: an efficient general purpose program for assigning sequence reads to genomic features. *Bioinformatics* 30, 923–930 (2014). [PubMed: 24227677]
72. Beber ME et al. eQuilibrator 3.0: a database solution for thermodynamic constant estimation. *Nucleic Acids Res.* 50, D603–D609 (2022). [PubMed: 34850162]
73. Waterhouse A. et al. SWISS-MODEL: homology modelling of protein structures and complexes. *Nucleic Acids Res.* 46, W296–W303 (2018). [PubMed: 29788355]
74. Hebditch M. & Warwicker J. Web-based display of protein surface and pH-dependent properties for assessing the developability of biotherapeutics. *Sci. Reports* 201991 9, 1–9 (2019).
75. Paz I, Kligun E, Bengad B. & Mandel-Gutfreund Y. BindUP: a web server for non-homology-based prediction of DNA and RNA binding proteins. *Nucleic Acids Res.* 44, W568–W574 (2016). [PubMed: 27198220]

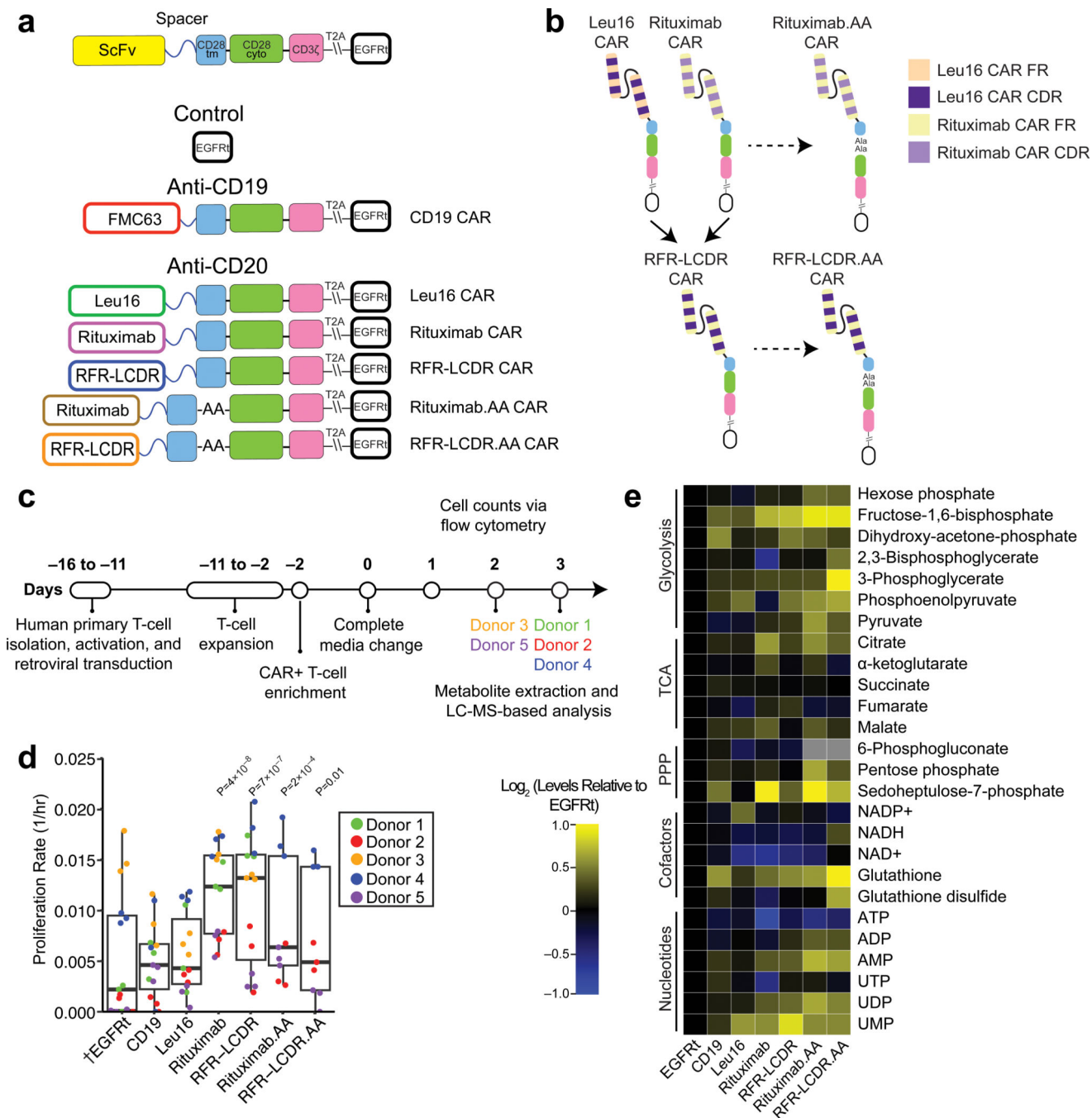


Figure 1: Construction, proliferation, and metabolome of CAR-T cells.

(a) CAR proteins consist of extracellular domains for antigen binding and intracellular domains for signaling. The scFvs, which determine antigen specificity, were derived from three monoclonal antibodies (FMC63, Leu16, and rituximab) and fused to extracellular spacers followed by CD28 transmembrane (tm) and cytoplasmic (cyto) domains as well as CD3 ζ signaling domain. Truncated EGFR (EGFRt) was co-expressed via a self-cleaving (T2A) peptide and used as a transduction marker. Two alanine residues were inserted between the transmembrane and intracellular domains in rituximab.AA and RFR-LCDR.AA

CARs. **(b)** RFR-LCDR CAR was constructed by hybridizing the framework regions (FRs) of rituximab and the complementarity-determining regions (CDRs) of Leu16. **(c)** The timeline marks T-cell isolation, transduction, expansion, and measurement of proliferation and metabolome. CAR-T cells were generated from human primary T cells between T-16 and T-11 days. T cells were enriched for CAR⁺ expression by magnetic-activated cell sorting and seeded in fresh RPMI + dFBS media on day 0. Cells were counted for 2 or 3 days, after which their metabolites were extracted for LC-MS analysis. **(d)** Proliferation rates were determined based on the changes in cell numbers between day 1 and the last time point for each donor's cells. T cells expressing rituximab-based (rituximab, RFR-LCDR, rituximab.AA, and RFR-LCDR.AA) anti-CD20 CARs grew faster than EGFRt control T cells. Each box shows the three quartiles (with the center line representing the median), and the whiskers extend to the minimum and maximum values that are within 1.5-fold of the interquartile range (n=9 or 15 biological replicates derived from up to five donors). Statistical significance was determined by two-tailed *t* tests for a linear mixed-effects model (see Methods) in reference to EGFRt control T cells (†). **(e)** CAR-T cells showed CAR-dependent metabolite abundances. Within each row, yellow and blue colors indicate higher and lower levels of a metabolite compared to EGFRt control T cells.

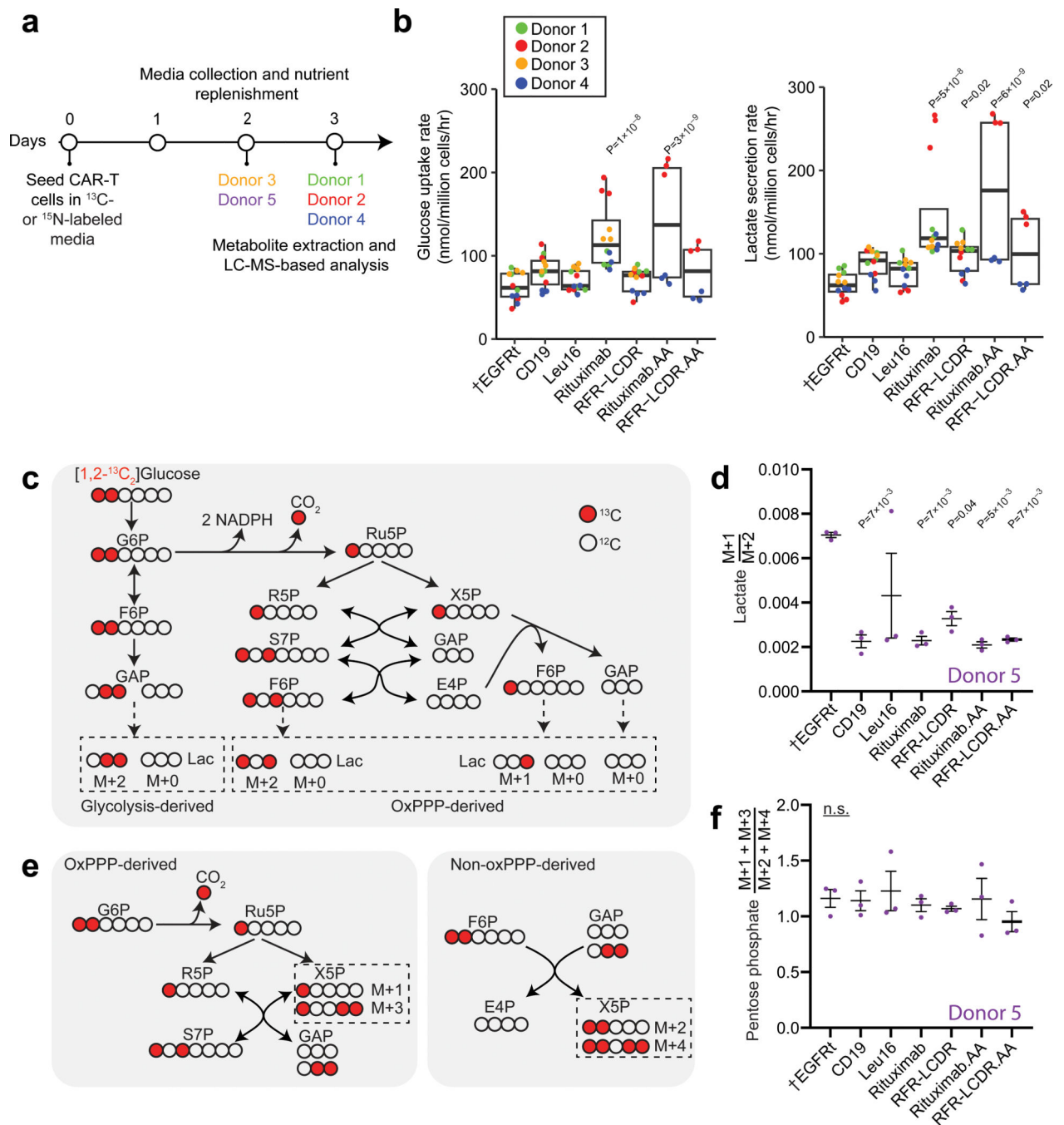


Figure 2: Glycolysis and pentose phosphate pathway (PPP) activity in CAR-T cells.

(a) The experimental timeline marks T-cell seeding in isotope-labeled medium, medium collection, and measurement of intracellular and extracellular metabolites. CAR-T cells were seeded in fresh ^{13}C - or ^{15}N -labeled media at $t=0$ hours. Media samples were collected for LC-MS analysis between day 1 and the last time point for each donor's cells, after which cells were also harvested for intracellular metabolite measurement. No media samples were collected for Donor 5. (b) Glucose uptake and lactate secretion rates in rituximab and rituximab.AA anti-CD20 CARs were elevated. Each box shows the three quartiles (with the

center line representing the median), and the whiskers extend to the minimum and maximum values that are within 1.5-fold of the interquartile range (n=6 or 12 biological replicates derived from up to four donors). **(c-f)** EGFRt T cells and CAR-T cells were cultured in media containing [1,2- $^{13}\text{C}_2$]glucose for 48 hours. **(c)** Singly ^{13}C -labeled (M+1) lactate is only generated through the oxidative PPP (oxPPP), while doubly ^{13}C -labeled (M+2) lactate comes from either glycolysis or oxPPP. **(d)** The (M+1)/(M+2) ratio indicates the activity of oxPPP relative to glycolysis. All but Leu16 CAR-T cells showed lower relative oxPPP activity than EGFRt control T cells. **(e)** Depending on its synthesis route (oxPPP or non-oxPPP), pentose phosphate contains odd or even numbers of ^{13}C atoms. Pentose phosphate M+1 and M+3 originate from oxPPP, whereas M+2 and M+4 originate from non-oxPPP. **(f)** The odd-to-even ^{13}C -labeling ratio of pentose phosphate indicated that the relative usage of oxPPP and non-oxPPP for the nucleotide precursor did not change with CAR expression. Panels (d) and (f) show the mean \pm the standard error of the mean (s.e.m.) with n=3 biological replicates from Donor 5. Statistical significance of glucose uptake and lactate secretion rates was determined by two-tailed *t* tests for a linear mixed-effects model (see Methods) in reference to EGFRt control T cells (\dagger). Statistical significance of labeling measurement was determined by one-way analysis of variance (ANOVA) followed by Tukey's multiple comparison test in reference to EGFRt control T cells (\dagger). n.s. indicates no statistical significance.

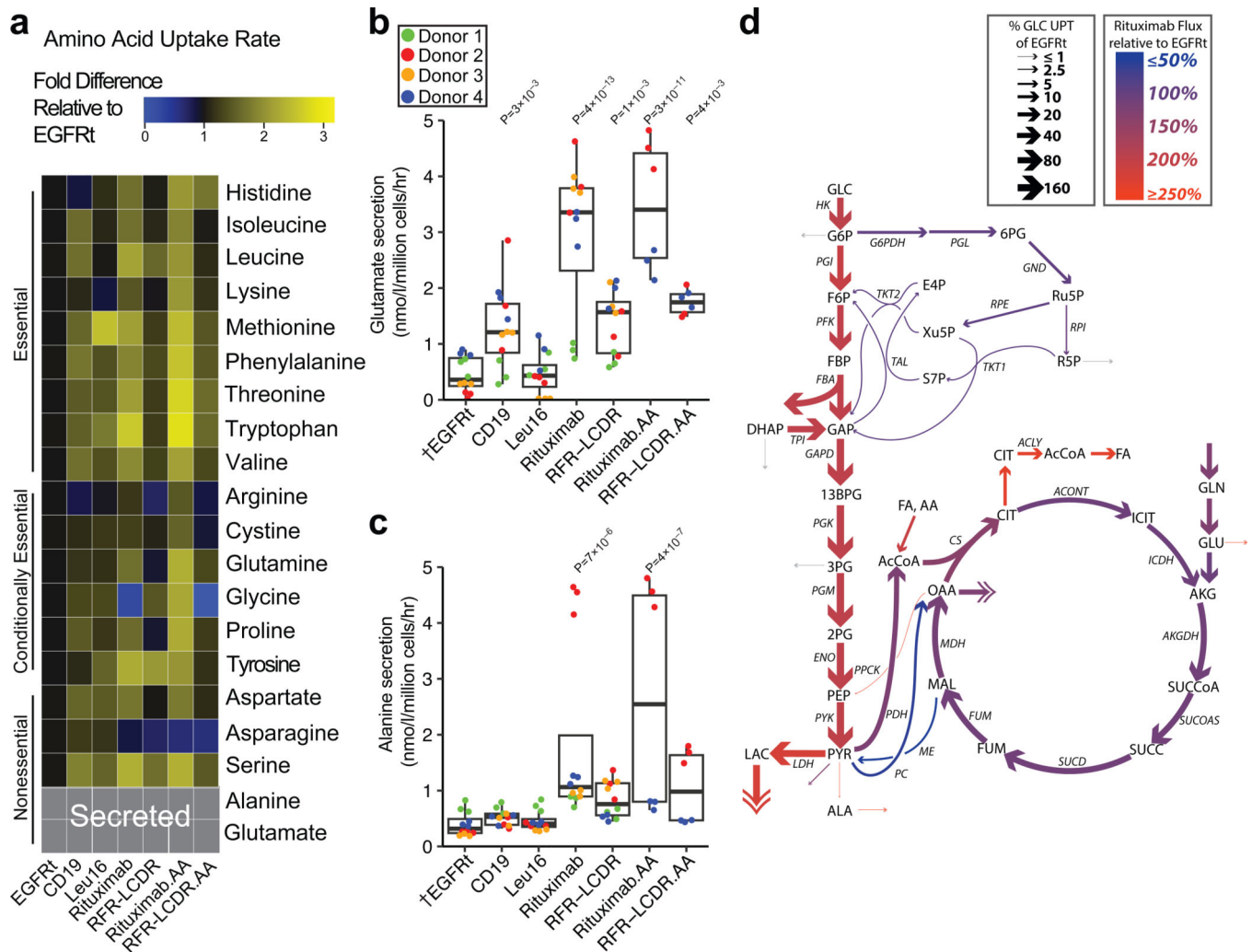


Figure 3: Rituximab-based CD20 CARs increase T-cell metabolic fluxes.

(a) Amino acid uptake rates were mostly elevated in CAR-T cells compared with EGFRt control T cells. The data represent the mean of measurements from Donors 1–4 cells. (b) Glutamate secretion rates were faster in anti-CD19 and rituximab-based anti-CD20 CAR-T cells compared to the EGFRt control T cells. (c) Rituximab and rituximab.AA CAR-T cells secreted alanine significantly faster than EGFRt control T cells. Each box in (b) and (c) shows the three quartiles (with the center line representing the median), and the whiskers extend to the minimum and maximum values that are within 1.5-fold of the interquartile range ($n=6$ or 12 biological replicates from up to four donors). (d) Metabolic fluxes through central carbon metabolism were compared between EGFRt control T cells and rituximab anti-CD20 CAR-T cells, which showed the largest differences in uptake and secretion rates as well as isotope labeling patterns (Extended Data Fig. 4). Metabolic flux analysis was performed using nutrient uptake rates, byproduct secretion rates, and intracellular metabolite labeling patterns in cells that were fed $[1,2-^{13}\text{C}_2]$ glucose, $[\text{U}-^{13}\text{C}_6]$ glucose, or 50% $[\text{U}-^{13}\text{C}_5-^{15}\text{N}_2]$ glutamine, which were obtained from Donors 1–6 cells (see Methods). Arrow widths represent the magnitudes of fluxes, normalized to glucose uptake (GLC UPT), for EGFRt T cells. Red and blue colors indicate higher and lower fluxes in rituximab

CAR-T cells with respect to EGFRt control T cells, while gray indicates low-confidence flux shifts. Statistical significance for glutamate and alanine secretion in panels (b) and (c) was determined by two-tailed t tests for a linear mixed-effects model (see Methods) in reference to EGFRt control T cells (†).

Author Manuscript

Author Manuscript

Author Manuscript

Author Manuscript

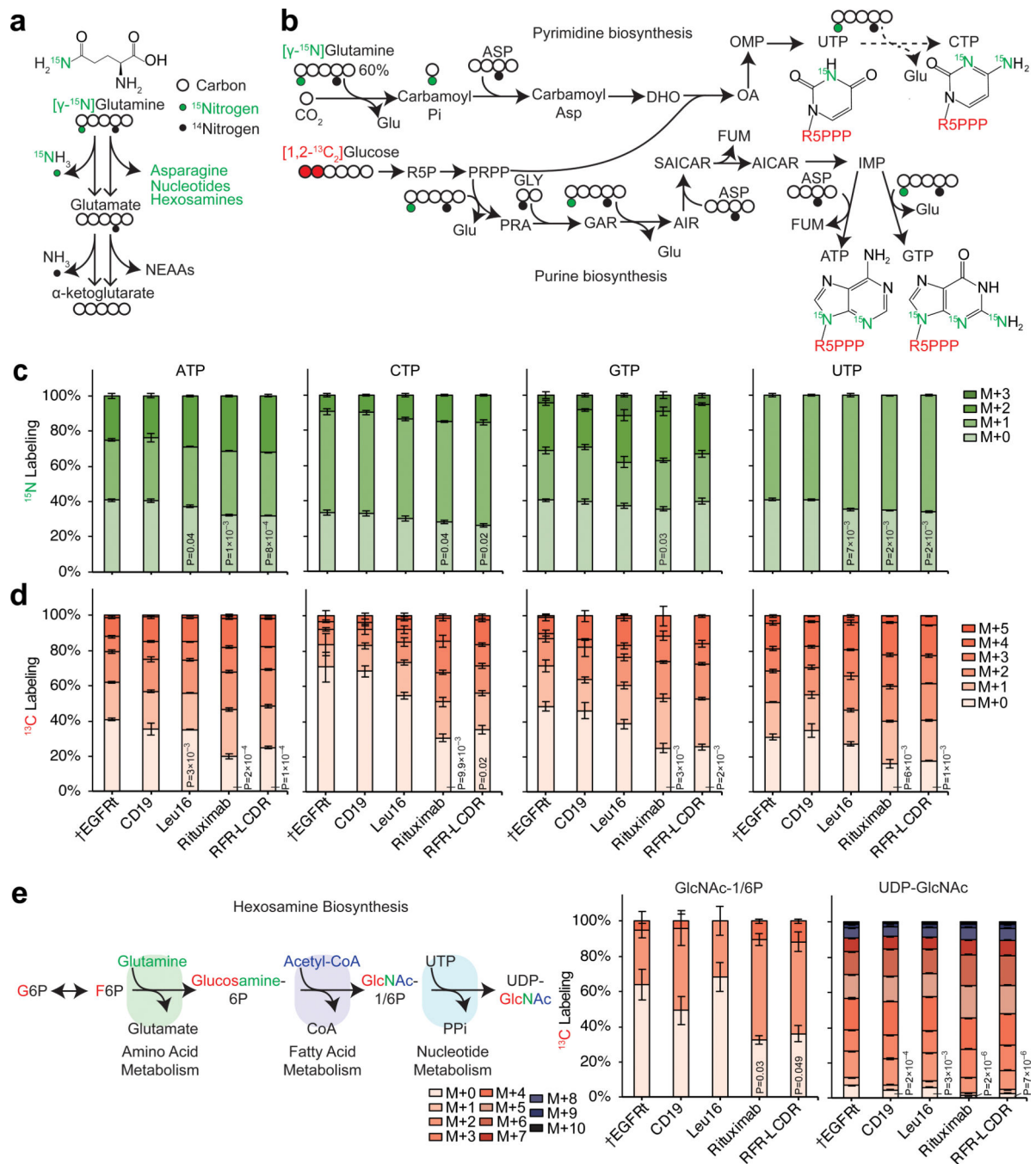


Figure 4: Tracing nitrogen and carbon in nucleotide and hexosamine biosynthesis.

(a) The fates of ^{15}N in $[\gamma\text{-}^{15}\text{N}]$ glutamine include ammonia, asparagine, nucleotides, and hexosamines. (b) Nucleotide biosynthesis map shows how stable isotopes of $[\gamma\text{-}^{15}\text{N}]$ glutamine and $[1,2\text{-}^{13}\text{C}_2]$ glucose are incorporated into pyrimidines and purines. (c) EGFRt T cells and CAR-T cells from Donor 4 were cultured in media containing 50% $[\gamma\text{-}^{15}\text{N}]$ glutamine for 72 hours. Nucleotides were labeled more in anti-CD20 CAR-T cells, especially those with rituximab and RFR-LCDR CARs, than in EGFRt control T cells. (d-e) EGFRt T cells and CAR-T cells from Donor 5 were cultured in media containing

[1,2-¹³C₂]glucose for 48 hours. **(d)** Nucleotides were labeled more in rituximab and RFR-LCDR CAR-T cells than in EGFRt control T cells. The greater labeling fractions in the same (48- and 72-hour) time periods indicated faster nucleotide turnover in rituximab and RFR-LCDR CAR-T cells than in EGFRt control T cells. **(e)** Hexosamine biosynthesis pathway incorporates glucose carbons and glutamine nitrogen into pathway intermediates. N-acetylglucosamine-1/6-phosphate (GlcNAc-1/6P) and UDP-N-acetylglucosamine (UDP-GlcNAc) were labeled more in rituximab and RFR-LCDR CAR-T cells than in EGFRt control T cells, indicating their increased turnover in the CAR-T cells. ¹³C-labeling fractions were corrected for natural isotope abundance and impurities. Panels (c-e) show the mean ± s.e.m. with n=3 biological replicates. Statistical significance was determined by two-tailed *t* test in reference to EGFRt control T cells (†) for M+0 labeling.

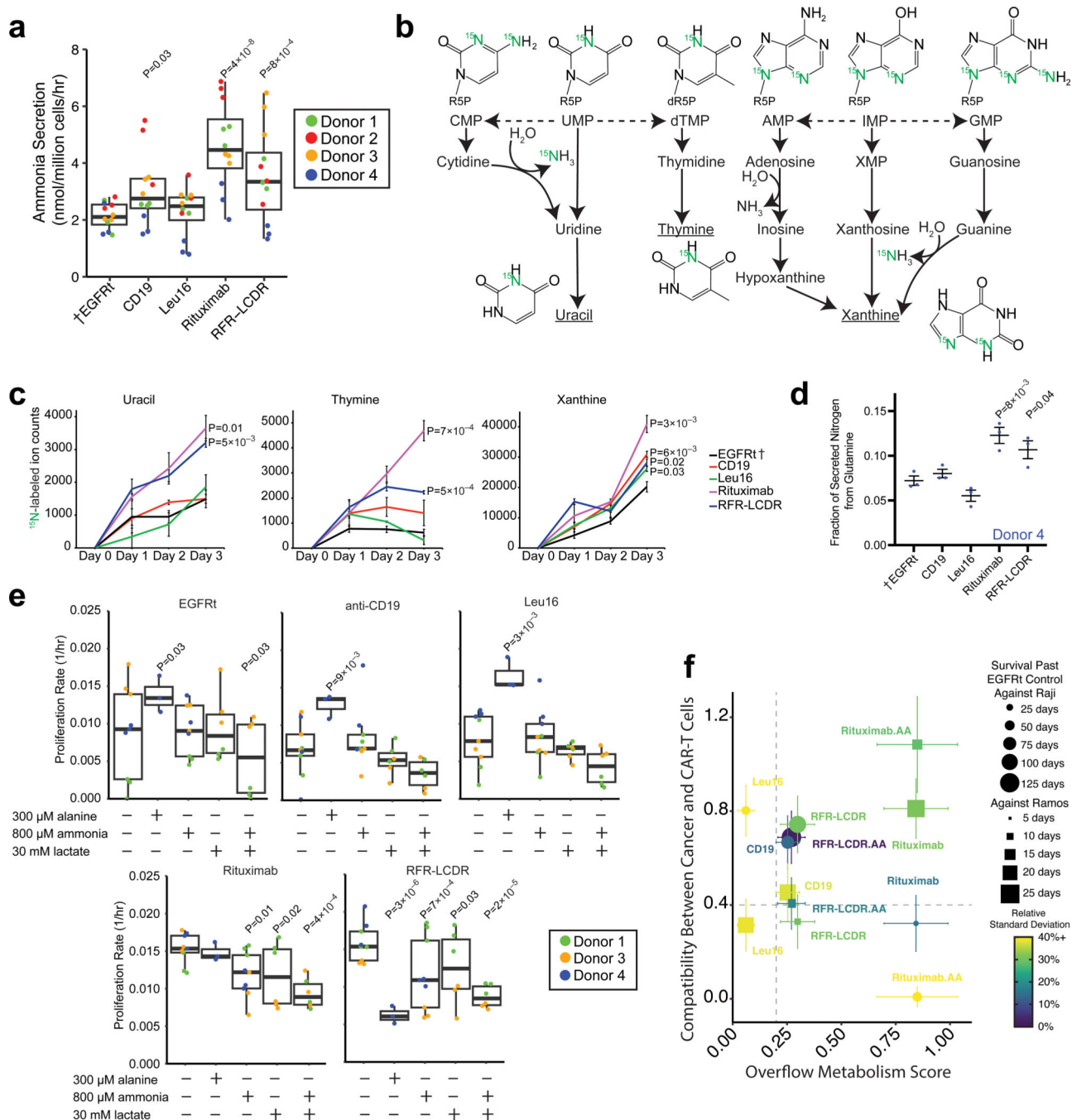


Figure 5: Overflow metabolism and metabolic compatibility.

(a) Ammonia secretion rates of CAR-T cells were measured. Each box shows the three quartiles (with the center line representing the median), and the whiskers extend to the minimum and maximum values that are within 1.5-fold of the interquartile range (n=12 biological replicates from four donors). (b) Nucleotide degradation pathway shows the fates of ^{15}N from $[\gamma\text{-}^{15}\text{N}]$ glutamine to nucleobases. Uracil, thymine, and xanthine (underlined) were secreted by T cells. (c) EGFRt and CAR-T cells from Donor 4 were cultured in media containing 50% $[\gamma\text{-}^{15}\text{N}]$ glutamine for 72 hours. ^{15}N -labeled pyrimidine and purine

nucleobases were measured from media samples collected each day. **(d)** The fractions of glutamine-derived nitrogen that were secreted as glutamate, alanine, ammonia, and nucleobases were calculated from uptake and secretion rates. **(e)** Proliferation rates for EGFRt control T cells and CAR-T cells grown in media containing alanine, ammonia, and/or lactate to mimic the tumor microenvironment. Each box shows the three quartiles (with the center line representing the median), and the whiskers extend to the minimum and maximum values that are within 1.5-fold of the interquartile range (n= 3, 6, or 9 biological replicates from up to three donors). **(f)** The *in vivo* efficacy of CAR-T cells was plotted with corresponding metabolic compatibility between cancer and CAR-T cells and overflow metabolism score of CAR-T cells (see Supplementary Note 1). Plot shows the mean \pm s.e.m. with n=6 or 12 biological replicates. The marker sizes and colors represent the mean and the relative standard deviation of the days that tumor-bearing mice (n=6 animals) survive with respective CAR-T cell treatment. Gray lines are visual guides for separating efficacious treatment groups. Statistical significance in panels (a) and (e) was determined by two-tailed *t* tests for a linear mixed-effects model (see Methods) in reference to EGFRt control T cells (\dagger) for ammonia secretion and the control media condition for proliferation rates for each cell type. Panels (c) and (d) show the mean \pm s.e.m. with n=3 biological replicates, and statistical significance was determined by two-tailed *t* tests in reference to EGFRt control T cells (\dagger).

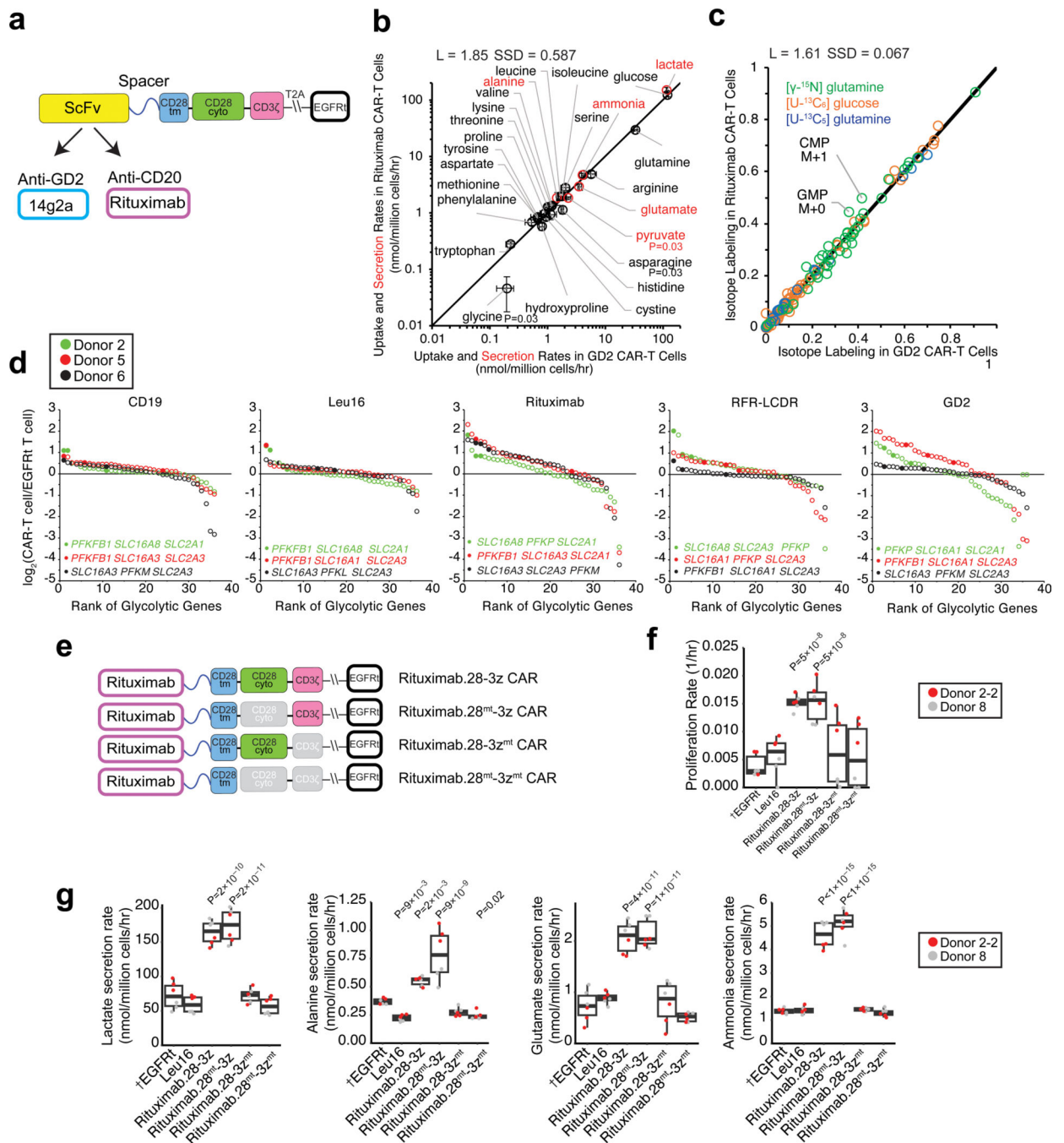


Figure 6: Mechanistic insights into unexpected hypermetabolism in CAR-T cells.

(a) The 14g2a-based anti-GD2 (GD2) CAR was constructed similarly to the rituximab anti-CD20 CAR, with the scFv as the only difference. (b) Rituximab anti-CD20 CAR-T cells from Donors 1–4 and GD2 CAR-T cells from Donors 3 and 4 displayed similar rates of nutrient uptake (black) and byproduct secretion (red). SSD is the sum of squared differences, and L is the total distance between individual points and the line of unity. Plot shows the mean \pm s.e.m. with $n=6$ or 12 biological replicates. Statistical significance was determined by two-tailed t test. (c) Metabolites in rituximab and GD2 CAR-T

cells, which were fed [γ - ^{15}N]glutamine, [U - $^{13}\text{C}_6$]glucose, or [U - $^{13}\text{C}_5$]glutamine, were labeled similarly. Metabolites with a distance of at least 0.05 are labeled. The transport fluxes and isotope labeling patterns revealed that GD2 CAR-T cells were metabolically most similar to rituximab CAR-T cells (*cf.* Extended Data Fig. 7). **(d)** Glycolytic gene expression in CAR-T cells relative to EGFRt control T cells is rank ordered with filled dots representing the highest ranked isoform involved in each of the three rate-determining steps of glycolysis: glucose import (*SLC2A1* and *SLC2A3*), phosphofructokinase (*PFKL*, *PFKM*, *PFKP*, *PFKFB1*, and *PFKFB3*), and lactate export (*SLC16A1*, *SLC16A3*, *SLC16A7*, and *SLC16A8*). **(e)** Three mutants of rituximab CAR were generated to disable the phosphorylation of CD28 and/or CD3 ζ signaling domains: rituximab.28^{mt}-3z, rituximab.28-3z^{mt}, and rituximab.28^{mt}-3z^{mt}. **(f)** Proliferation rates of CAR-T cells were determined based on the cell number changes over time. Donor 2-2 represents a second batch of transduced cells from Donor 2. **(g)** The secretion rates of lactate, alanine, glutamate, and ammonia in mutant rituximab anti-CD20 CAR-T cells were compared to those of EGFRt control, Leu16 CAR-, and rituximab CAR-T cells. Each box in panels (f) and (g) shows the three quartiles (with the center line representing the median), and the whiskers extend to the minimum and maximum values that are within 1.5-fold of the interquartile range (n=6 biological replicates from two donors). Statistical significance was determined by two-tailed *t* tests for a linear mixed-effects model (see Methods) in reference to EGFRt control T cells (\dagger).